FRICTION STIR BLIND RIVETING OF DISSIMILAR MATERIALS

A DISSERTATION SUBMITTED TO THE GRADUATE DIVISION OF THE UNIVERSITY OF HAWAI‘I AT MĀNOA IN PARTIAL FULFILLMENT OF THE REQUIREMENT FOR THE DEGREE OF

DOCTOR OF PHILOSOPHY

IN

MECHANICAL ENGINEERING

MAY 2017

By

Wei-Ming Wang

Dissertation Committee:

Jingjing Li, Chairperson
Mehrdad N. Ghasemi Nejhad
Lloyd H. Hihara
Scott F. Miller
Tao Yan

ACKNOWLEDGEMENT

I sincerely appreciate my advisor, Dr. Jingjing Li, for her valuable advice throughout my graduate studies. I wish to thank her for her advices, encouragement, and support.

I would like to extend my appreciation to my advisory committee members, Dr. Nejhad, Dr. Hihara, Dr. Miller, and Dr. Tao for their valuable responses. I would also like to thank Dr. Hihara for preparing the exposed samples and Dr. Miller for the suggestions about numerical model.

I would like to thank Dr. Eric Hellebrand for teaching me to operate SEM. I thank my friends, Yingsen Tang, Sladjan Lazarevic, Kaimiao Liu, and Haris Khan for their help and suggestions in my research.

I thank my families for their understanding and support.

ABSTRACT

Joining of dissimilar materials receives great attentions to broaden the implementation of lightweight components for vehicle applications. Friction stir blind riveting (FSBR), as a newly developed method, shows potentials in joining dissimilar metals and thermoplastic composites for complex structures. In this process, a rotating blind rivet is applied to soften and penetrate two workpieces with frictional heat. The rotation stops after the head of blind rivet contacts the top surface of workpiece, and then the mandrel is pulled up and breaks off at the setting force.

Finite element is one of the best technique to observe material flow and temperature during a friction stir process; nevertheless, the main issue to simulate FSBR process is the large deformation of work materials. Therefore, FEM coupled with smoothed particle hydrodynamics (SPH) was utilized to simulate FSBR process for joining magnesium and aluminum alloys. To validate the model, plunge force and torque were compared to experimental measurements. The history of temperature, von Mises stress, and material flow of workpieces are available in this SPH-FEM model.

To broaden the application of FSBR, the knowledge of mechanical properties and failure mechanisms of FSBR joints is required. Three optimal configurations of FSBR lap joints, including aluminum, magnesium, and a carbon-fiber reinforced polymeric composite (CFRP), were studied in this dissertation. *In situ* nondestructive testing method, acoustic emission (AE), was applied to identify the deformation zone and failure mode of FSBR lap joints under uniaxial tensile loading. Scanning electron microscopy (SEM) was also performed to analyze the fractured microstructures.

Post-corrosion mechanical behavior of dissimilar material joints is a primary consideration for their applications subjected to a corrosive environment. In this study, it was found that for CFRP constituent exposed joints, the dominated failure mode was tension failure and there was no loss in strength observed under current corrosion condition; however, exposed Mg/Al joints depicted a complex failure mechanism where failure was caused by bearing force and secondary bending during tensile tests, and degradation in strength was observed.

TABLE OF CONTENETS

LIST OF TABLES

LIST OF FIGURES

CHAPTER 1

INTRODUCTION

1.1 Research motivation

With increasing demands of joining dissimilar materials for new structures or parts with tailored properties, efficient joining technologies are of extensive interest. This is particularly true for automotive sector, where improving the ability to join dissimilar materials will speed up the application of lightweight materials such as carbon fiber reinforced plastic composites and aluminum in structures thereby help to reduce mass and CO_2 emissions. However, dissimilar materials joining presents challenges significantly different than similar materials joining because of their different mechanical, thermal and chemical properties.

Friction stir blind riveting (FSBR) is a new one-sided mechanical joining technology. FSBR combines the strength of both friction stir riveting (FSR, a joining method invented at GM [1]) and blind riveting (BR) with four main steps (Fig. 1.1): (a) a commercial blind rivet is approaching the work material under high speed rotating; (b) the rivet is driven into the work materials under reduced penetration force by utilizing the generated frictional heat; (c) the mandrel is pulled upward once the blind rivet is fully inserted; and (d) the mandrel is broken to lock the two sheets together and thus the form the final joint (as a BR process) [2].

For this new technique, there is limited research on the characterization of joint properties. Mechanical behavior is one of the interest. It is also noticed that the effect of corrosive environment on dissimilar material joint cannot be ignored especially when different materials form galvanic corrosion due to the electropotential difference. To study this complex friction stir process, numerical analysis is an efficient tool to quantify the properties that cannot be easily accessed through experiment, such as material flow, strain distribution and temperature changes. This information is helpful to understand the joint formation and resultant structures.

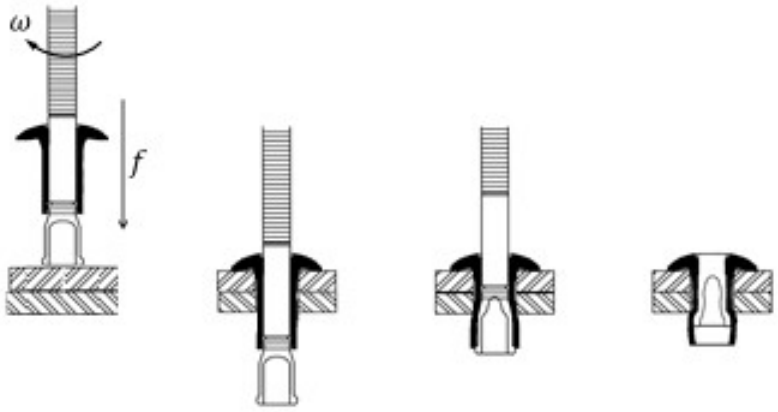

Figure 1.1 Four stages of FSBR process [1]

1.2 Background of friction stir processes

Several friction stir processes have been applied in joining dissimilar metals. Friction stir welding (FSW), a widely investigated process, was first invented in 1991[3]. In this process, a rotating tool softens, stirs, and mixes the metals along the interface between the two materials. This process was applied to form dissimilar joint between 5052 aluminum and AZ31 magnesium alloy in 2011[4].

As a variation of FSW, friction stir spot welding (FSSW) is used to connect two materials through a small "spot." In this process, the work materials are placed overlapped to each other, and the rotating tool plunges from the top to the second material. The upper sheet must be softer than the lower sheet in FSSW process to allow lower sheet to pierce into the upper sheet [5]. Since the material flow is important for FSSW joint, researchers studied the material flow of FSSW in several ways. One of the simple methods is to place a copper foil on the top surface of the upper metal sheet or at the interface of two metal sheets before FSW process [6]. Therefore, researchers can observe the metal flow patterns through the copper foil deformations. Finite element method (FEM) has been used to simulate FSSW process and observe the metal flow and generation of mechanical interlocking [7]. They confirmed that the size and formation of hook-shape interlock depended on the shape of tooling, welding times and temperatures; and the temperature is related to spindle speeds and feed rates.

Friction stir forming (FSF) is another joining process for dissimilar materials. In the process, two work materials are overlapped to each other, where the bottom sheet has a predrilled hole. The top material is softened by frictional heat generated from high-speed rotating tool, and pushed through the predrilled hole in bottom sheet, which forms the joint through mechanical locking [8].

1.3 Research objectives

The aim of this research is to understand the FSBR process, and mechanical behavior of dissimilar FSBR joints. The specific tasks are:

1. To develop a numerical model for FSBR process. The force, torque, material flow, and temperature in FSBR process have not been studied in simulations. These four elements are related to whether a FSBR joint succeeds or fails.
2. To identify different materials and laying up sequences effect the mechanical behavior of FSBR joints, including the failure modes and joint strength.
3. To investigate the effects of corrosive environment on dissimilar FSBR joints.

1.4 Organization of dissertation

In this dissertation, a numerical model is created for FSBR process in Chapter 2. The smooth particle hydrodynamics (SPH) elements were applied on workpieces to overcome the challenges in simulating large deformations and distortions which are usually involved in friction stir process. The model was validated by comparing thrust forces from the numerical prediction and experimental results. This model can predict the temperature and displacement histories, and material flow, strain and stress, which further help to understand the process physics.

Chapter 3 focuses on investigating the different failure mechanisms of as-fabricated FSBR joints under quasi-static tensile loading. Three different materials with three stacking sequences were selected. Acoustic emission was applied to monitor the damage initiation and evolution during the quasi-static tensile tests. To receive more information on the failure modes,

fractographic analysis was also performed. Based on the above analyses, distinct failure modes and damage accumulation processes were identified for FSBR dissimilar material joints.

Chapter 4 investigates the effects of marine environment on mechanical properties and failure modes of FSBR dissimilar materials joints under tensile load. Three FSBR dissimilar joint configurations were considered. The dominated failure modes and fracture surfaces of the corrosive samples were compared with the as-fabricated samples discussed in Chapter 2. The loss of nominal stiffness of exposed joints was also examined.

Chapter 5 is conclusion and future work.

REFERENCES

[1] R. Stevenson and P.-C. Wang, "Friction stir rivet drive system and stir riveting methods". United States of America Patent 6988651 B2, 24 January 2006.

[2] "BRALO," Baralo, [Online]. Available: http://www.bralo.com/ckfinder/archivos/files/03.INFORMACION%20TECNICA/CATALOGO 2013.pdf. [Accessed 12 4 2014].

[3] Colligan, K. "Material flow behavior during friction welding of aluminum." Welding journal vol. 75, no. 7, pp. 229s-237s, 1999.

[4] Y. Yan, D.-t. Zhang, C. Qiu and W. Zhang, "Dissimilar friction stir welding between 5052 aluminum alloy and AZ31 magnesium alloy," Transactions of Nonferrous Metals Society of China, vol. 20, pp. s619-s623, 2010.

[5] S. Bozzi, A. L. Helbert-Etter, T. Baudin, B. Criqui and J. G. Kerbiguet, "Intermetallic compounds in Al 6016/IF-steel friction stir spot welds," Materials Science and Engineering: A, vol. 527, no. 16-17, pp. 4505-4509, 2010.

[6] Q. Yang, S. Mironov, Y. S. Sato and K. Okamoto, "Material flow during friction stir spot welding," Materials Science and Engineering: A, vol. 527, no. 16-17, pp. 4389-4398, 2010.

[7] S. Hirasawa, H. Badarinarayan, K. Okamoto, T. Tomimura and T. Kawanami, "Analysis of effect of tool geometry on plastic flow during friction stir spot welding using particle method," Journal of Materials Processing Technology, vol. 210, no. 11, pp. 1455-1463, 2010.

[8] S. Lazarevic and S. F. Miller, "Experimental analysis of friction stir forming for dissimilar material joining application," Journal of Manufacturing Processes, vol. 15, no. 4, pp. 616-624, 2013.

CHAPTER 2

NUMERICAL ANALYSIS OF FRICTION STIR BLIND RIVETING OF MAGNESIUM AND ALUMINUM ALLOYS

2.1 Introduction

Unlike traditional blind riveting, friction stir blind riveting (FSBR) is one joining technology that utilizes frictional heat to weld materials [1-2]. In brief, the blind rivet can penetrate the workpiece due to material softening by the friction between rivet and workpiece. Once the blind rivet head touches the upper surface of workpiece, the mandrel is pulled up and broken automatically, which is the same process as traditional blind riveting.

There are several ways to observe the material flow and temperature evolution during the friction stir process. To study the temperature evolution in the workpiece, traditional methods are using an infrared camera or thermocouples; however, the observation area is limited using these methods. Observing the changes of joint cross-sectional microstructure is one optical way to study material flow [3-4]. To track the microstructure changes, some researchers proposed to put a thin layer of foil at the interface of two workpieces [5-6]. Also, metal powder is another proposed method to trace the material flow by place the metal powder at the interface [7]. However, these introduced methods cannot be applied to determine the material flow and temperature evolution simultaneously. Numerical analysis is a feasible method to investigate stress, material flow and thermal distribution during friction stir process without high-tech equipment.

Although there are some publications about FSBR process, the numerical analysis related to FSBR process is limited. Some researchers utilized finite element method (FEM) to analyze the thermo-mechanical behavior of friction stir welding, friction stir spot welding, and friction stir drilling process [8-12]. Nevertheless, it is found that FEM has drawbacks to simulate the friction stir process due to the large deformation and distortion of meshes. Although these drawbacks can be overcome by remeshing (adaptive) and/or eroding elements, these solutions have a

disadvantage, i.e. the adaptive remeshing cannot track the changes of certain elements due to the remeshed elements and nodes being renumbered. Moreover, eroding elements represent a part of mass in system that are removed, which is proper for drilling simulation (cut off materials) but not suitable for friction stir process.

Some researchers proposed a mesh free method, smooth particle hydrodynamics (SPH), to study metal cutting [13-15] and friction stir process [16-17]. The plunge part of FSW process can also be studied by SPH method [18]. The physical domain of SPH method is described by particles and Kernel function, which is used to derive approximated solution [19]. The first advantage of SPH method is that the simulation is more "nature" than FEM model in friction stir process since SPH model does not refine or delete elements. Additionally, SPH model can track the displacement and temperature of any element. Since SPH model is computationally expensive, the tool (regard as a rigid body) in simulation can be a FEM model due to the fact that SPH method is also based on Lagrangian method (nodes used to label material points and mesh deformed with material). In this study, LS-DYNA software was utilized to simulate the thermal-mechanical behavior of workpieces in FSBR process. To decrease the computational time, the SPH-FEM partial model was applied.

2.2 Methods for friction stir processes

Compared to the simulation of FSW processes, FSBR has two characteristics making it more difficult to simulate. First, the shape of blind rivet is more complex than friction stir welding tool. Second, in this process, two different materials were considered and being contacted with blind rivet at different moments. The SPH method is helpful in dealing with the large deformation and blending of the two materials. This section presents the theories and considerations for SPH-FEM simulation of FSBR process.

2.2.1 Thermal-mechanical relationship

The relationship between temperature and mechanical properties is an important consideration in all friction stir processes. The equation of thermal conduction is

$$\rho C_p \frac{\partial T}{\partial t} = k\nabla^2 T + \left(q_f + q_d\right) \quad (1)$$

where ρ is density, C_p is heat capacity, T is temperature, t is time, k is thermal conductivity, q_f is the heat generation rate due to friction, and q_d is heat generation rate from plastic deformation.

Assume q_f is based on Coulomb's law, then the heat generation rate from friction can be represented as:

$$q_f = \pi d S \mu F \quad (2)$$

where d is diameter of contact surface, S is rotational speed of rivet, μ is coefficient of friction, and F is normal force.

The heat generation rate from plastic deformation is

$$q_d = \beta\sigma\dot{\varepsilon}_p \quad (3)$$

where β is inelastic heat fraction, σ is stress, and $\dot{\varepsilon}_p$ is plastic strain. The inelastic heat fraction is often assumed as 0.9 for metals [20-21].

2.2.2 Johnson-Cook method and material properties

Several material models have been applied in friction stir process. Recently, thermal dependent properties method [22] and Johnson-Cook method are the two most used models in numerical analysis. Johnson-Cook method was selected in this simulation because of the available material properties.

The Johnson-Cook is represented by the following equation:

$$\sigma = [A + B(\varepsilon^p)^n][1 + C\ln(\dot{\varepsilon}^p)]\left[1 - \left(\frac{T - T_{room}}{T_{melt} - T_{room}}\right)^m\right] \quad (4)$$

where σ is stress, ε^p is effective plastic strain, $\dot{\varepsilon}^p$ is effective plastic strain rate, T is working temperature, T_{room} is room temperature, and T_{melt} is melting temperature. A, B, n, C, and m are parameters collected from mechanical tests.

The two materials utilized in this study are magnesium alloy (AZ31b) and aluminum alloy (AA5754). Table 2.1 shows the material properties of these two materials, and Table 2.2 lists the Johnson-Cook parameters. The Johnson-Cook parameters of Mg and Al in this study are from [23] and [24], respectively.

Table 2.1 Material properties of magnesium and aluminum alloys

	Mass Density (g/cc)	Shear Modulus (GPa)	Melting Temperature (°C)	Heat Capacity (J/g-°C)	Thermal Conductivity (W/m-K)
AZ31b	1.77	17	610	1	96
AA5754	2.66	25.9	600	0.9	125

Table 2.2 Johnson-Cook parameter of magnesium and aluminum alloys

	A	B	n	C	m
AZ31b [23]	225.171	168.346	0.242	0.013	1.55
AA5754 [24]	160	279	0.3436	0.039137	1.6687

2.2.3 Element types for friction stir blind riveting

Traditionally, the numerical model of friction stir process is accomplished by conventional meshing methods, such as Lagrangian, Eulerian, and Arbitrary Lagrangian-Eulerian (ALE) methods. However, the severe mesh distortion can cause error termination of the simulation. Although remeshing and eroding methods can prevent the error, the results will be inaccurate when the deformation is severe. In addition, utilizing the eroding function to represent the history (displacement, temperature, and so on) of elements is not available. Therefore, SPH approach, a Lagranggian mesh-free method, was selected.

The particle domain in SPH approach can simulate a large deformation without mesh problems and track the history of any element. In this approach, the kernel approximation is used to derive the weak form of motion equation for SPH model. The kernel approximation can be presented by the following equation (1-D domain):

$$f(x) \approx \int_{\Omega} f(x')W(x - x', h)\, dx' \tag{5}$$

where $f(x)$ is the field function at position x, x' represents position of particle in the integration domain Ω, $W(x - x', h)$ is a smoothing kernel function, and h is the smoothing length [19]. The SPH equation of motion (weak form) can be derived by applying equation (5) into the strong form of equation of motion. Figure 2.1 illustrates the 2-D domain of smoothing function for a particle. The letter κ is a constant for smoothing length, which is 2 in this study.

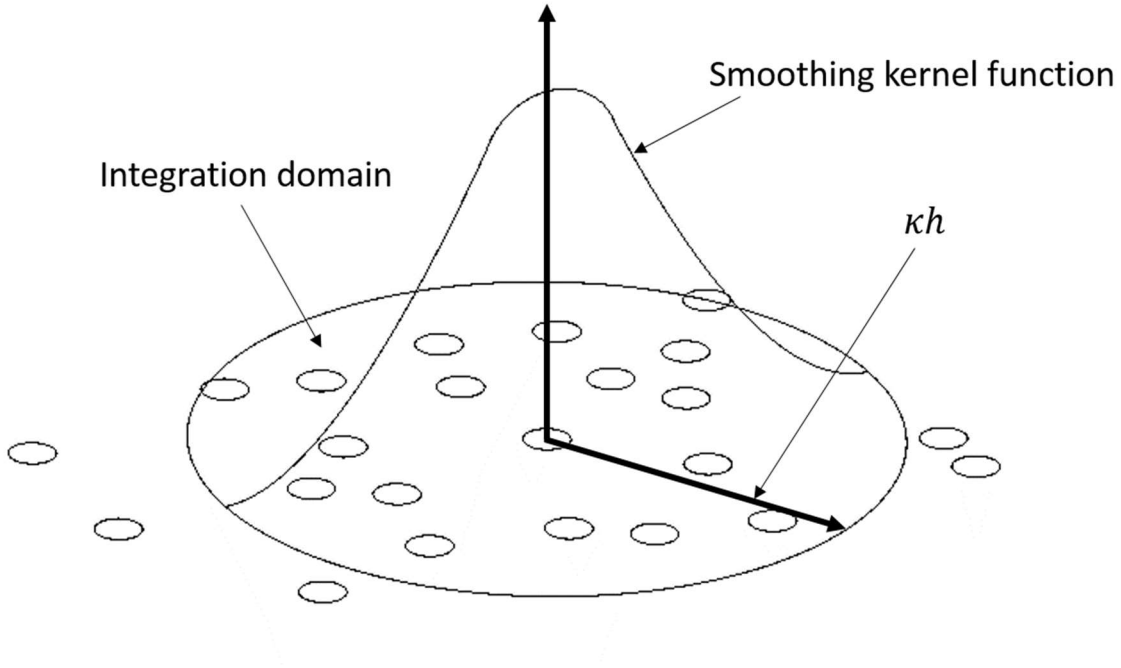

Figure 2.1 Domain of SPH model

2.2.4 SPH-FEM model development

Ls-Dyna was selected as simulation solver in this research. The numerical model for FSBR process was created by coupled FEM (blind rivet) and SPH (workpieces) models. The material model of blind rivet was rigid body. The contact type between FEM and SPH model was node to surface, whereas the contact between two SPH models was not necessary. The friction coefficient between blind rivet and Mg alloy was assumed as 0.25, and friction coefficient between blind rivet and Al alloy was assumed as 0.15. These two friction coefficients assumed to be constant during the process. The feed rate of blind rivet was 120 mm/min and spindle speed was 5000 rpm. The room temperature was 22 °C. The total simulation time was 2 seconds, where the travel depth of tool was 4 mm. The simulation time was sufficient to observe the workpiece deformations and material flow.

There are four main challenges to apply SPH method in this study. The first challenge was that computation could be very expensive. Moreover, the geometry of the blind rivet is complex compare to the tool of FSW or FSSW, which means FSBR model needs finer and more elements than FSW and FSSW models to create the workpieces. Therefore, to find a way to speed up the simulation is necessary. The traditional speed-up method (e.g. changing mass scale) for FEM model did not work for the SPH model. In this study, the model failed once it used mass scale. Other researchers also found that mass scaling is not a way to reduce calculation time of SPH model [25]. Some researchers studied the effect of changing time scale to speed up the simulation metal cutting [13, 25]. To use this method, the feeding speed of tool is multiplied by a number and the total time is divided by the same number in simulation. However, changing time scale may not be a proper method for friction stir process since the frictional heat and heat transfer are important in friction stir process. To reduce the computational time, 2-D model is also a selection for axisymmetric models. However, 2-D model does not have control on the friction between tool and workpieces. It can only assume the tool generates heat over time to soften workpieces. The temperature is difficult to predict since the contact surface of blind rivet is complex. Therefore, a 3-D SPH-FEM model was used in this study, where the model has a thickness in x direction to integrate the frictional effect and heat flux in x-y plane. The displacement in x direction is constrained. Figure 2.2 illustrates the SPH-FEM model. The model length (y-direction) was 6mm. The thickness of Mg alloy and Al alloy in z direction were 1.7

mm and 3.5 mm. The thickness in x direction was 0.17 mm. All SPH elements were fixed in x direction. Moreover, a partial blind rivet model (5 mm in length) was used.

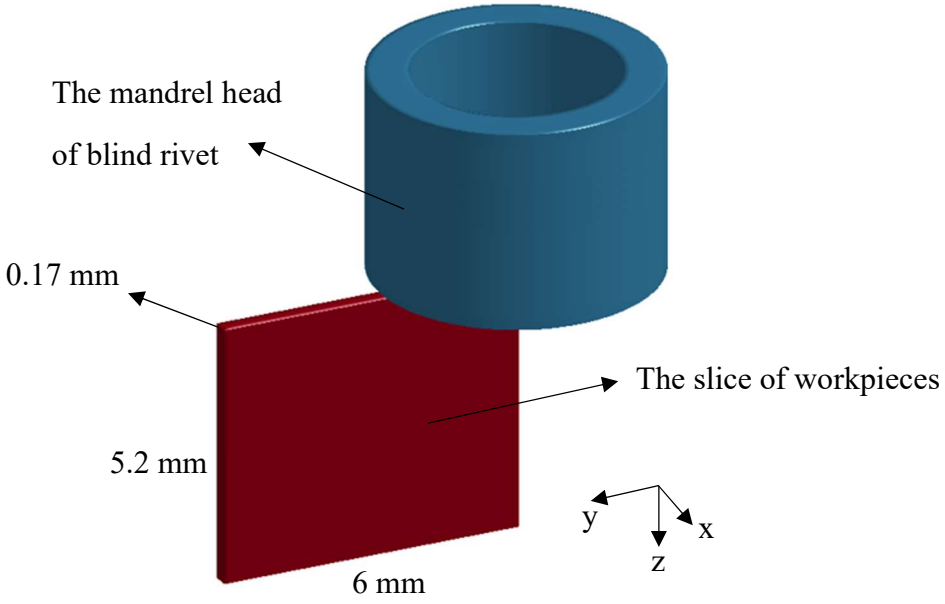

Figure 2.2 The illustration of SPH-FEM model

Heat transfer was the second challenge. There is no heat convection between SPH model and the surroundings, i.e. there is no heat transfer between SPH and FEM parts [26]; therefore, the simulation accuracy may be affected. This influence can be solved or decreased by utilizing a large workpiece model to dissipate heat. However, this will increase the computational cost. Therefore, the heat flux function was applied for this model. The heat flux q can be represented as:

$$q = -k\frac{\mathrm{T}_i - \mathrm{T}_o}{dx_w} \tag{6}$$

where k is thermal conductivity, T_i is the temperature of the element i which is at the heat flux boundary in the model, as circled in Figure 2.3, T_o is room temperature, and dx_w is distance between the boundary element i and ambience. Assume the model is big enough to dissipate heat

during the process, $T_o = 22$ °C and $dx_w = 0.17$ mm (i.e. the distance between two adjacent SPH nodes) were used in the simulation. The heat fluxes from the top and bottom surfaces to the air were also calculated from equation (6). The thermal conductivity was assumed as 0.025 W/m-K. Using heat flux function is another reason to apply 3-D model. The heat flux direction is normal to a surface of four nodes. Therefore, at least two elements in x direction is necessary. Figure 2.3 shows the boundary conditions of the FEM-SPH model.

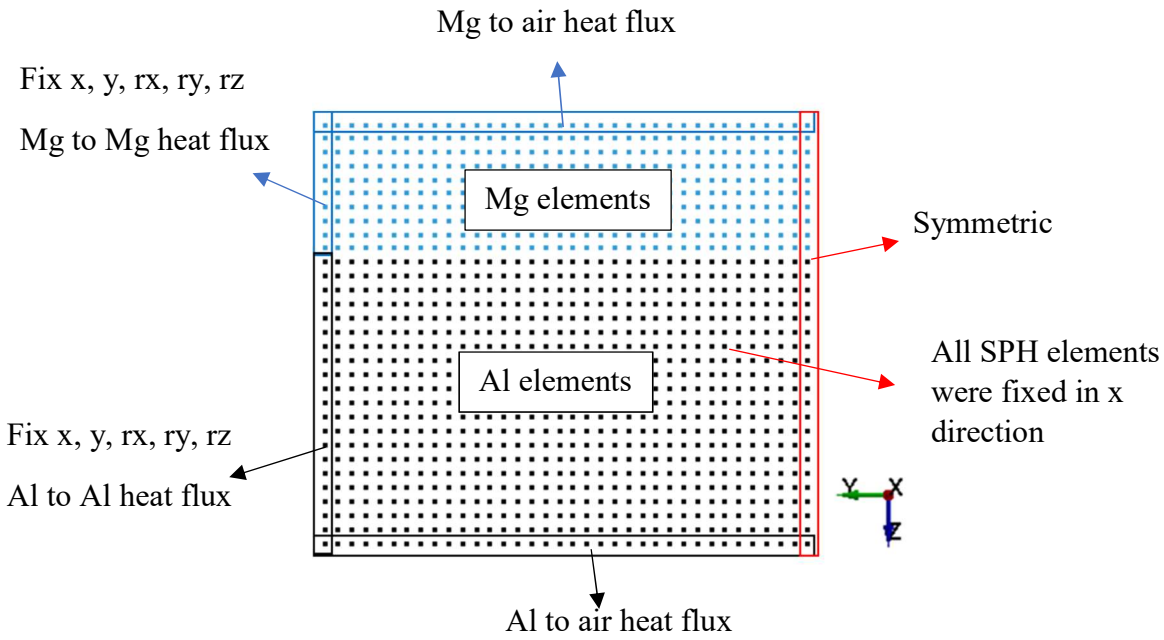

Figure 2.3 Boundary conditions of workpieces

The third challenge is contact problem. In friction stir welding, the tool contacts both workpieces at the same time; in friction stir spot welding, the tool is mainly plunged into the top layer. Both processes mainly have SPH-FEM elements contact. To simulate a tool plunging into two SPH models sequentially is difficult since both contact types (SPH-FEM and SPH-SPH) use different contact methods. Usually, a SPH element is created from the center of an eight-node solid element. Nevertheless, the boundary of the model is not correct (Fig. 2.4 a) and therefore the tool cannot attach to the workpiece at the right time, which means temperature will not increase before the tool contacts the SPH elements. One way to solve this issue is to give the

SPH elements a volume (Fig. 2.4 b). By this way, SPH elements are not nodes but spheres when contacting with FEM elements. Nevertheless, this did not work for the tool with complex geometry. Renormalization function in LS-DYNA can improve the contact result [27] but leads to a longer computational time. In this study, the SPH elements were created from the nodes of solid elements (Fig. 2.4 c). Since the boundary nodes were at the right positions, the friction between blind rivet and top sheet started at the right time. By this approach, the load-time curve of simulation matched the experiment results when the blind rivet penetrated the top material (Mg alloy). When both top and bottom SPH models were created from the nodes of solid elements, the interface between the two workpieces had both Mg and Al SPH elements. This is an issue for a SPH part to SPH part contact. The interaction between two SPH parts is through SPH interpolation functions, and there is no external force between two SPH parts. In other words, two SPH parts are treated as one. Therefore, when the interface has both Mg and Al SPH elements in the beginning of simulation, the interface became a different layer which is stronger than either Mg or Al alloy. The model of workpieces was bended significantly once the blind rivet arrived at the interface, and the simulation result was misleading at the same time. To solve this problem, the Mg elements at interface layer were removed and the Al elements were kept for contacting with blind rivet. The influence of removing the elements on interface was small when the mesh size was small enough.

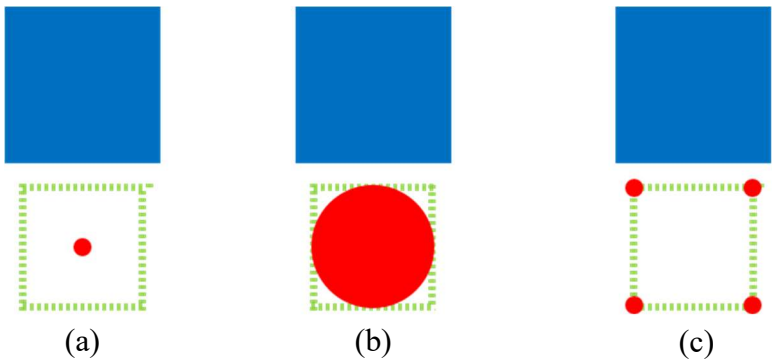

Figure 2.4 SPH elements created by (a) center of solid elements, (b) center of solid elements with volume, and (c) nodes of solid elements.

The forth issue is that the performance of SPH model is instable under tension loading, which will cause the model to fail. Therefore, a rigid shell was added at the bottom of Al model in this study. The properties of AA5754 were applied on this shell part. Since the simulation focuses on the first two seconds of FSBR process, the effect of this shell part is assumed to be ignorable. However, it should be noticed that this method cannot be utilized for simulating the blind rivet totally penetrates bottom workpieces since the bottom of model has a rigid body.

2.3 Experimental setup

The experiments were set up for collecting the plunge force and torque during FSBR process. The experimental results were compared with the simulation results in next section for validation. The computer numerical control (CNC) bridge machine center was utilized to conduct FSBR experiment. The feed rate of blind rivet was 120 mm/min and spindle speed was 5000 rpm. A 1.7 mm Mg alloy sheet was on a 3.5 mm Al alloy sheet and both materials were fixed by a fixture, where the dynamometer for force and torque measurement were connected under the fixture. The maximum diameter of mandrel was 6.4 mm. The mandrel of blind rivet was made of carbon boron steel with zinc coating.

2.4 Validation of plunge force and torque

In this section, the contact load and torque were applied to validate simulation results. For the SPH-FEM simulation, the plunging time was set 2 seconds to make sure the blind rivet can pass through interface of both materials completely. It is found that the load-time curve has two main peaks and it can be divided into three areas. The load curve in first area was from the contact of blind rivet and Mg alloy sheet which provided the first peak. The second area was created by the contact of blind rivet and both Mg and Al alloy sheets, which can be identified in the numerical model. The second area started at 0.87 s when the contact force of tool and Al began, and stopped at 1.3 s when the contact force of tool and Mg became zero. In third area, the loading curve was mainly from the contact between blind rivet and Al sheet. Figure 2.5 shows the experimental force/torque curve and the identified areas following above definitions. It can be

seen that load curve indeed can be divided into three different areas and fits the simulation results well, implying that the contact time of blind rivet and both material is correct in this model.

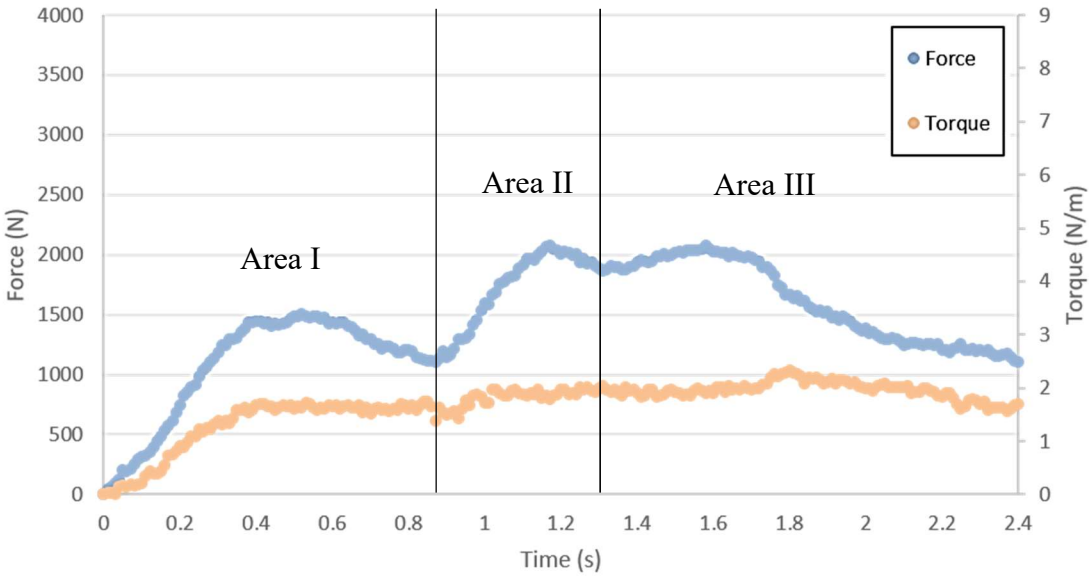

Figure 2.5 Contact situations of experiment results identified by numerical model

To compare the simulation results with experimental measurements, a geometry coefficient is needed because e the experimental measurements are based on the whole workpieces while the simulation results are only based on the partial workpieces; The geometry coefficient G for this partial model is:

$$G_t = \frac{\frac{(D_o + D_i)}{2}\pi}{t_x} \tag{7}$$

where D_o and D_i are outer and inner diameters of blind rivet, respectively. t_x represents the model thickness of workpieces in x direction. In equation (7), D_o is 3.18 mm, D_i is 2.1 mm, and t_x is 0.17 mm. Figure 2.6 and 2.7 illustrate the comparison of simulated plunge force and torque with experimental ones, where two experimental results are included. It is found that the simulation results agree with the experimental ones.

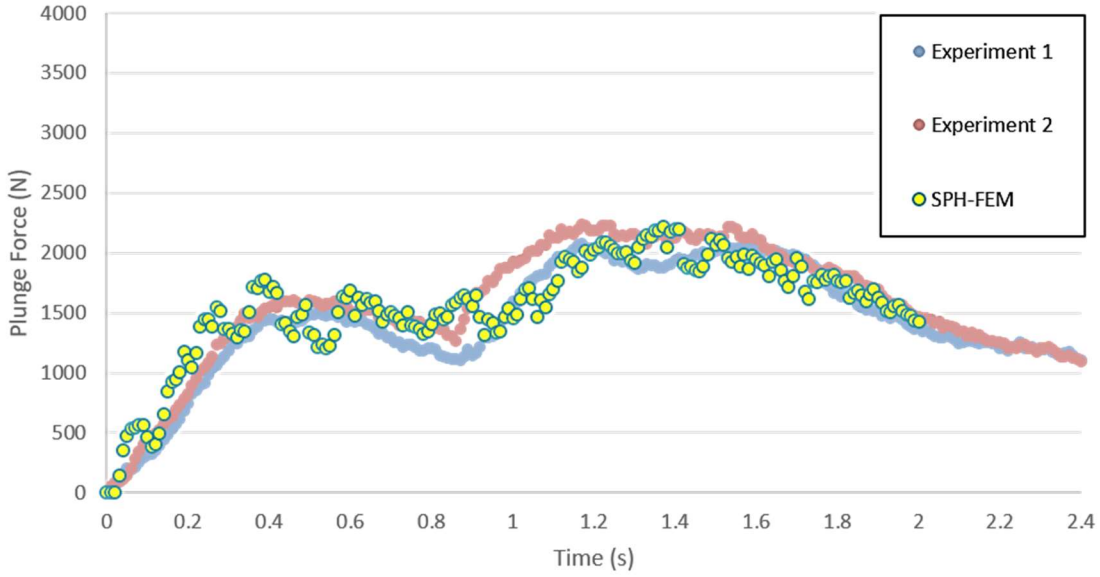

Figure 2.6 Validation of plunge force

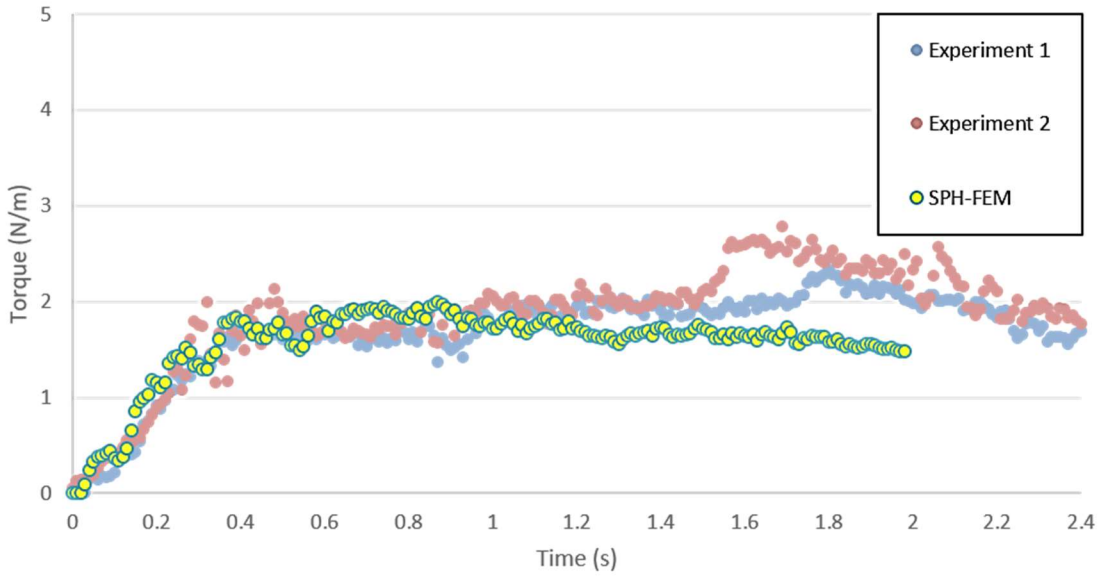

Figure 2.7 Validation of torque

Fig. 2.8 illustrates a typical comparison of experimental and simulation results near the interface of workpieces. The shape of interface was used to validate the numerical model. Because the deformation at interface mostly ended around 1.4 s in simulation, the shape at interface remained almost unchanged during 1.4 s to 2.0 s. Fig. 2.8 is based on the simulation result at 2.0 s and the experimental result, which is a complete FSBR joint. Both experimental and simulation results showed Al sheet penetrating Mg sheet at the area near the rivet body. The shape and size in both results were close. Therefore, this numerical model provided the approximate result of deformation at interface.

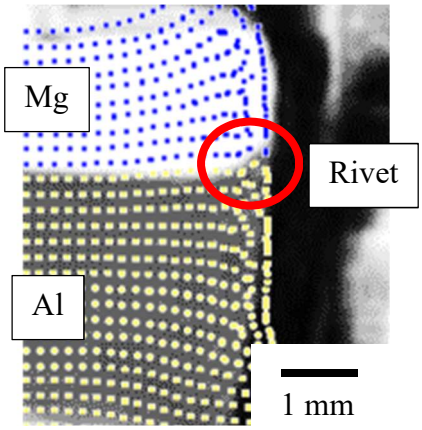

Figure 2.8 Comparison of experimental and simulation results

In addition, the use of infrared camera (FLIR IR camera SC655) was attempted to validate this model. However, it is found that the resolution of pictures is not high enough because the infrared camera cannot be put close to the samples due to the limitation of experimental setup. Moreover, the SPH model size is 6 mm in radial direction and only about 2.82 mm is visible (3.18 mm blocked by blind rivet). In the picture from infrared camera, the ratio of rivet diameter and the width of picture is about 2:127 (the rivet body diameter is 6.5 mm), and the number of pixels of the picture is 640 (width) x 480 (height), therefore the number of pixels in the area of 2.82 mm can be calculated as:

$$\frac{2}{127}\times 640\times \frac{2.82}{6.5}\approx 4.4 \tag{8}$$

The result shows only 4 pixels in 2.82 mm. For these reasons, the infrared camera cannot provide the detailed temperature distribution to validate this SPH model.

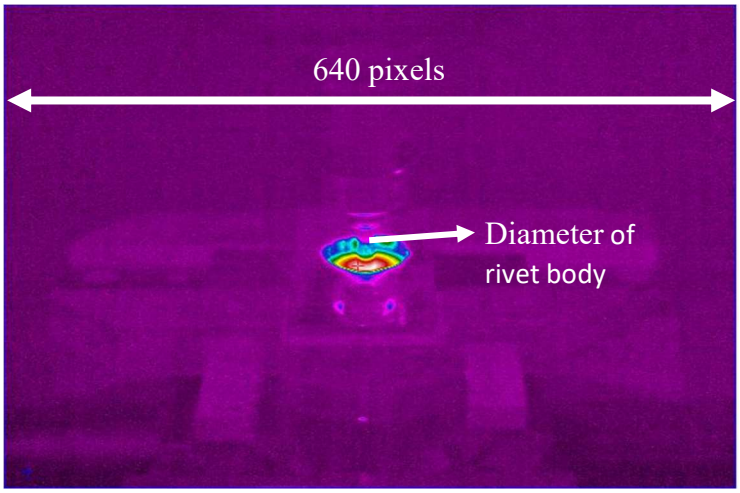

Figure 2.9 Measured temperature distribution using the infrared camera

2.5 FSBR simulation results

From the SPH-FEM model, the temperature evolution, stress distribution, and material flow can be obtained simultaneously, which are difficult to be measured from experiments. In this section, these information during the FSBR process are presented in detail. Besides, the joint cross-sectional microstructure is observed to validate the simulated material flow.

2.5.1 Temperature

As presented in Section 2.4, the plunge process can be divided into three different stages, i.e. penetrating Mg, interface, and Al. Figure 2.10 shows the temperature distribution at 0.5 s, 1.0 s, and 1.6 s to compare the temperature changes under these stages, where the corresponding plunge depth at these moments are 1.0 mm, 2.0 mm, and 3.2 mm, respectively. At 0.5 s, the highest temperature is about 570 °C in Mg alloy (Fig. 2.10 a). The maximum temperature during the FSBR process is found around 1.0 s, where Mg and Al reach around 620 °C and 540°C,

respectively (Fig. 2.10 b). Although the blind rivet travels into Al sheet at this moment, the highest temperature is still found in Mg sheet. The highest temperature observed at 1.6 s is about 590 °C, which is in Al sheet. The zone with highest temperature at 1.6 s is located at outer area which is right next to tip. The inner area right next to tip (curve area) has the second highest temperature (~ 570 °C).

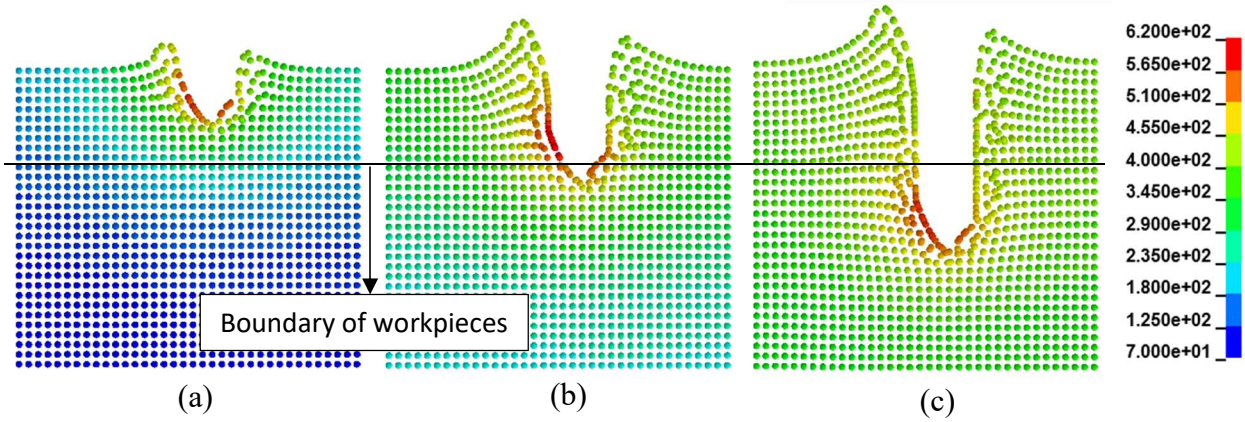

Figure 2.10 Temperature distribution of FSBR process at (a) 0.5 s, (b) 1.0 s, and (c) 1.6 s

It is known that the melting temperatures of Mg and Al alloy are 610 °C and 600 °C, respectively. Form the temperature evolution under different plunge stages, it can be concluded that Mg sheet reaches melting temperature and Al sheet is close to the melting temperature in this model.

2.5.2 von Mises stress

The distributions of von Mises stress under different plunge stages are shown in Figure 2.11. The maximum stress during the whole process (310 MPa) can be found at about 0.1 s, localized at the contact surface of blind rivet and Mg alloy. This is because the temperature at contact surface is not high enough. The stress becomes lower after 0.2 s due to the softening of Mg sheet by frictional heat. In the period of 0.1 s to 1.0 s, the maximum stress decreases from 310 MPa to 190 MPa. However, from 1.0 s to 1.6 seconds, the maximum stress rises to 250 MPa. In this

period, the rivet is in the beginning stage of penetrating Al sheet and the temperature of contact surface increases. It should be noted that the maximum stress occurs in Al sheet and the stress in Mg is decreased continually. After 1.6 s, the maximum stress decreases again due to the increasing temperature at contact surface. It should be noticed that the bottom rigid body will affect the distribution results more once the blind rivet is close to the bottom area. At inner side of blind rivet (blind hole), some Mg elements are found to travel into Al sheet for about 0.56 mm at 2.0 s. These elements have highest von Mises stress at 1.6 s (Fig. 2.11 d) because their large deformation and displacement.

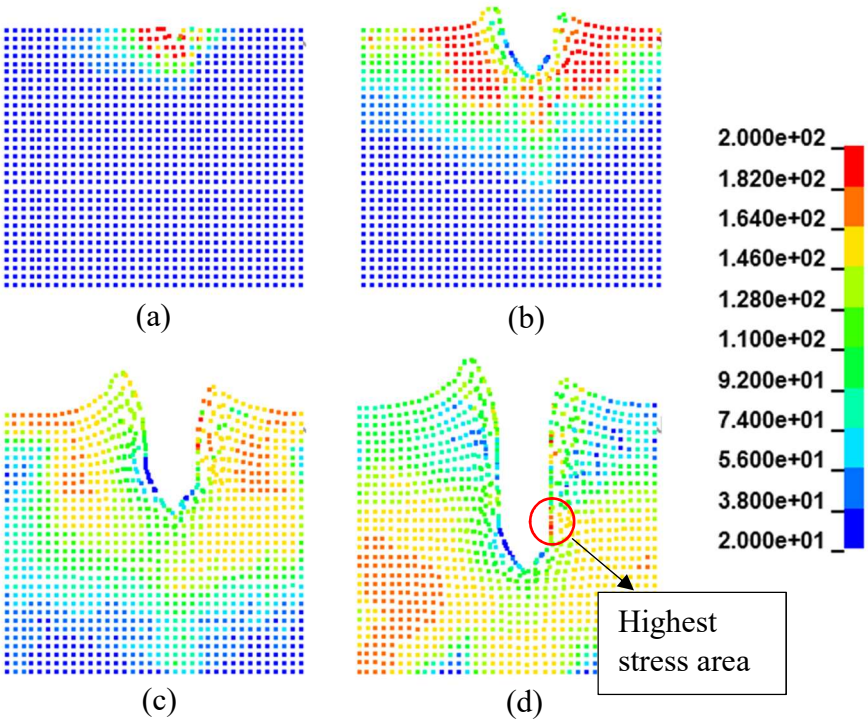

Figure 2.11 Distribution of von Mises stress at (a) 0.1 s, (b) 0.5 s, (c) 1.0 s, and (d) 1.6 s

2.5.3 Material flow

Material flow is an important indicator during the friction stir process since it can improve (mechanical interlocking) or decrease (defects) the strength of joints. Figure 2.12 shows the displacements of elements at 0.5 s, 1.0 s, and 1.6 s. The unit in scale bar is mm. It is found that the moving of elements close to outside surface are in similar direction, which creates bushing.

There is another bushing caused by the elements close to the inside surface. Also, the curve area at inside surface and right next to tool tip has different material flow, and some elements in this area have material rotation at 0.5 s (Fig. 2.12 a). This phenomenon is also found when the curve area reaches the interface area (Fig 2.12 b). As shown in Fig. 2.12 (c), the rotation of material flow at the curve area is not as significant as rotations at 0.5 s and 1.0 s, and material flow has different direction at 1.6 s. Besides, the level of material displacement in Al sheet is not as significant as that in Mg sheet.

For FSSW, material rotation is located near the shoulder of tool [28], which could create caves inside workpieces and these caves will decrease the strength of materials. However, for FSBR, the rotation area is found at the inner side of blind rivet. Therefore, whether the rotation area has caves or not does not affect the joint strength.

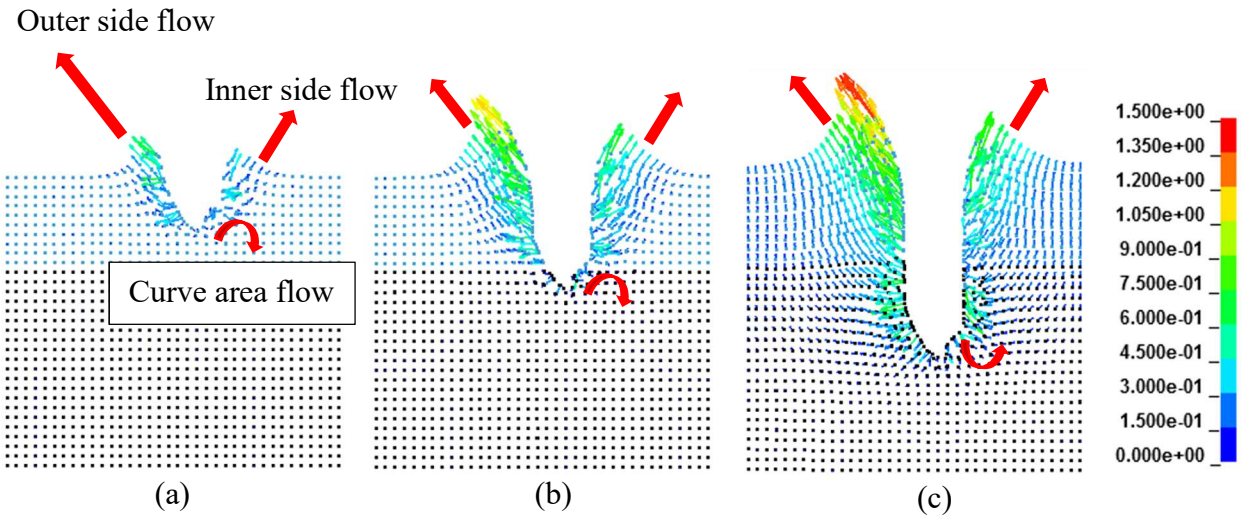

Figure 2.12 Element displacements (i.e. material flow) at (a) 0.5 s, (b) 1.0 s, and (c) 1.6 s

2.6 Conclusions

In this study, a 3-D model based on SPH method was applied to investigate material flow and temperature evolution in FSBR process. The simulated plunge force and torque were compared with experimental ones. The main conclusions are summarized as follows:

After tracking the temperature evolution during the FSRB process, it is found that Mg sheet at intersection area has reached the melting temperature (~610 °C) and Al sheet has not. From the SPH-FEM model, material rotation was found at inner area of blind rivet; therefore, it can be concluded that material rotation has not effect on the joint strength.

REFERENCES

[1] D. Gao, U. Ersoy, R. Stevenson and P.-C. Wang, "A New One-Sided Joining Process for Aluminum Alloys," ASME Journal of Manufacturing Science and Engineering, vol. 131, no. 6, 2009.

[2] J. Min, J. Li, B. E. Carlson, Y. Li, J. F. Quinn, J. Lin and W.-M. Wang, "Friction Stir Blind Riveting for Joining Dissimilar Cast Mg AM60 and Al Alloy Sheets," Journal of Manufacturing Science and Engineering, vol. 137, no. 5, 2015.

[3] W. Yuan, R. S. Mishra, B. Carlson, R. Verma and R. K. Mishra, "Material flow and microstructural evolution during friction stir spot welding of AZ31 magnesium alloy," Materials Science and Engineering A, vol. 543, pp. 200-209, 2012.

[4] G. Ma, "Friction-Stir Riveting: Characteristics of Friction-Stir Riveted Joints," Master thesis. Department of mechanical engineering, University of Toledo, 2012.

[5] Q. Yang, S. Mironov, Y. S. Sato and K. Okamoto, "Material flow during friction stir spot welding," Materials Science and Engineering A, vol. 527, pp. 4389-4398, 2010.

[6] W.-Y. Li, J.-F. Li, Z.-H. Zhang, D.-L. Gao and Y.-J. Chao, "Metal Flow during Friction Stir Welding of 7075-T651 Aluminum Alloy," Experimental Mechanics, vol. 53, pp. 1573-1582, 2013.

[7] Y.-C. Lin, J.-J. Liu and J.-N. Chen, "Material Flow Tracking for Various Tool Geometries During the Friction Stir Spot Welding Process," Journal of Materials Engineering and Performance, vol. 22, pp. 3674-3683, 2013.

[8] G. Buffa, J. Hua, R. Shivpuri and L. Fratini, "A continuum based fem model for friction stir welding—model development," Materials Science and Engineering A, vol. 419, pp. 389-396, 2006.

[9] C. Hamilton, S. Dymek and A. Sommers, "A thermal model of friction stir welding in aluminum alloys," International journal of machine tools and manufacture, vol. 48, no. 10, pp. 1120-1130, 2008.

[10] C. M. Chen and R. Kovacevic, "Finite element modeling of friction stir welding—thermal and thermomechanical analysis," International Journal of Machine Tools and Manufacture, vol. 43, no. 13, pp. 1319-1326, 2003.

[11] M. Miles, U. Karki and Y. Hovanski, "Temperature and Material Flow Prediction in Friction-Stir Spot Welding of Advanced High-Strength Steel," JOM, vol. 66, no. 10, pp. 2130-2136, 2014.

[12] S. F. Miller and A. J. Shih, "Thermo-Mechanical Finite Element Modeling of the Friction Drilling Process," Journal of Manufacturing Science and Engineering, vol. 129, pp. 531-538, 2007.

[13] A. A. Olleak, M. N. Nasr and H. A. El-Hofy, "The Influence of Johnson-Cook Parameters on SPH Modeling of Orthogonal Cutting of AISI 316L," in 10th European LS-DYNA Conference, Würzburg, 2015.

[14] V. Gylienė and V. Eidukynas, "The Numerical Analysis of Cutting Forces in High Feed Face Milling, Assuming the Milling Tool Geometry," Procedia CIRP, vol. 46, pp. 436-439, 2016.

[15] J. Limido, C. Espinosa, M. Salaün and J. L. Lacome, "SPH method applied to high speed cutting modelling," International journal of mechanical sciences, vol. 49, no. 7, pp. 898-908, 2007.

[16] A. Tartakovsky, G. Grant, X. Sun and M. Khaleel, "Modeling of friction stir welding (FSW) process with smooth particle hydrodynamics (SPH)," SAE Technical Paper, Vols. No. 2006-01-1394, 2006.

[17] S. A. Patil, "Modeling and characterization of spot weld material configurations for vehicle crash analysis," Doctoral dissertation. Wichita State University, 2014.

[18] S. Bhojwani, "Smoothed particle hydrodynamics modeling of the friction stir welding process," Master thesis. Department of mechanical engineering, University of Texas at El Paso, 2007.

[19] J. J. Monaghan, "Smoothed particle hydrodynamics," Annual review of astronomy and astrophysics, vol. 30, pp. 543-574, 1992.

[20] G. Ravichandran, A. J. Rosakis, J. Hodowany and P. Rosakis, "ON THE CONVERSION OF PLASTIC WORK INTO HEAT DURING," AIP conference proceedings, vol. 620, pp. 557-562, 2002.

[21] Y. Zhang, J. C. Outeiro and T. Mabrouki, "On the selection of Johnson-Cook constitutive model parameters for Ti-6Al-4V using three types of numerical models of orthogonal cutting," Procedia CIRP, vol. 31, pp. 112-117, 2015.

[22] M. Awang, V. H. Mucino, Z. Feng and S. A. David, "Thermo-Mechanical Modeling of Friction Stir Spot Welding (FSSW) Process: Use of an Explicit Adaptive Meshing Scheme," SAE Technical Paper, Vols. No. 2005-01-1251, 2005.

[23] D. Hasenpouth, "Tensile High Strain Rate Behavior of AZ31B Magnesium Alloy Sheet," Master thesis. Department of Mechanical Engineering, University of Waterloo, 2010.

[24] S. Suman, "mechanical properties of friction stir processed aa5754 sheet metal at different elevated temperature and strain rates," Mater thesis, Department of mechanical engineering, Indian institute of technology kharagpur, 2016.

[25] M. F. Villumsen and T. G. Fauerholdt, "Simulation of metal cutting using smooth particle hydrodynamics," in Tagungsberichtsband Zum-DYNA Anwenderforum Bamb, 2008.

[26] J. Xu, "Heat transfer with explicit SPH method in LS-Dyna," in Proceedings of 12th International LS-Dyna Users Conference, Dearborn, Michigan, 2012.

[27] C. Espinosa, J. L. Lacome, J. Limido, M. Salaun, C. Mabru and R. Chieragatti, "Modeling high speed machining with the SPH method," in 10th International LS-DYNA users conference, 2008.

[28] S. Horie, K. Shinozaki, M. Yamamoto and T. H. North, "Experimental investigation of material flow during friction stir spot welding," Science and Technology of Welding and Joining, vol. 15, no. 8, pp. 666-670, 2010.

[29] M. Movahedi, A. H. Kokabi, S. M. Seyed Reihani and H. Najafi, "Mechanical and Microstructural Characterization of Al-5083/St-12 lap joints made by friction stir welding," Procedia Engineering, vol. 10, pp. 3297-3303, 2011.

[30] A. A. M. Da Silva, E. Aldanondo, P. Alvarez, E. Arruti and A. Echeverria, "Friction stir spot welding of AA 1050 Al alloy and hot stamped boron steel (22MnB5)," Science and Technology of Welding and Joining, vol. 15, no. 8, pp. 682-687, 2010.

[31] W.-M. Wang, "Friction stir Blind riveting of CFRP and metals," Ph.D. qualify exam report, University of Hawaii at Manoa, 2014.

CHAPTER 3

CLASSIFICATION OF FAILURE MODES IN FRICTION STIR BLIND RIVETED DISSIMILAR MATERIAL LAP-SHEAR JOINTS

3.1 Introduction

Friction stir blind riveting (FSBR) is a one-sided mechanical joining technique aiming to assemble similar or dissimilar thermoplastic composites and metals that are softer than steel rivet [1-5]. Joining dissimilar materials is of increasing demand but limited by traditional joining methods such as fusion welding due to the different material melting temperatures and possible generation of intermetallic compounds. FSBR is a promising technique for overcoming the challenges in joining dissimilar materials by integrating the advantages of both friction stir riveting (FSR, a joining method invented at GM [1]) and blind riveting (BR). FSBR requires no surface preparation, predrilling hole, complex tool settings or long cycle times, which makes it particularly suitable for mass production.

The failure mechanisms were mostly investigated for various similar material mechanical joints. The basic failure mechanisms of the riveted joints for metals are, for example, net section failure, shearing of plate margin, large hole deformation, rivet failure, and rivet pull out; [6] and the failure modes of carbon fiber composites include net tension, shear-out, bearing, cleavage, tearing [7-8], fastener pull-through, and fastener failure [8]. Secondary bending of lap joints were studied [9-11], where the overlap length and material thickness are the two most important parameters for tensile strength [9], fatigue life [10], and out-of-plane failure modes [11].

Acoustic emission (AE) has been widely investigated because of its advantages in real time non-destructive monitoring of damage development. However, it is challenging to distinguish different damage modes through AE signals. Several studies have revealed that the history plots of AE amplitude and hit counts [12] and the signal energy (integration of the area under AE amplitude curve versus time) were able to identify the damage mechanisms for lay-up

composites [13]. AE was applied to detect matrix cracking, interphase failure, and fiber breakage for unidirectional glass fiber and carbon fiber reinforced laminates with static and dynamic tensile testing [14]. Some other methods such as fuzzy C-means clustering [15] and Kohonen's map [16] were compared with the history plot of hit counts to identify the failure patterns for composites. Accumulative AE hits and amplitude signals showed the feasibility in monitoring the damage patterns and failure progresses of mechanically fastened composite joints [17].

This section focuses on different mechanisms which lead to failure in FSBR joints based on three different material combinations through fractographic and AE analysis.

3.2 Manufacturing and experimental setup

The FSBR lap joints were first fabricated on a computer numerical control (CNC) machine. During the tensile tests, an AE senor was placed near the joint, which yielded additional information on defect development. The coming sections give details of the materials and the various manufacturing / experimental setups used during the study.

3.2.1 Materials and blind rivet

Aluminum (AA5754-O), magnesium (AZ31B-H23), and injection molded CFRP (Polyamide 66 matrix with 40 vol.% randomly oriented carbon fibers with a length of 300 – 500um) were selected in this study. Mechanical properties of these materials are listed in Table 3.1.

The commercial blind rivet used in FSBR was made of steel (body) and carbon boron steel (mandrel) with zinc coating, where the mandrel tip diameter was 6.4 mm, shoulder diameter was 6.5 mm, and the available penetration contact length was 23.7 mm.

Table 3.1 Joint geometries and mechanical properties

Materials	Size (mm^3)	Yield Strength (MPa)	Tensile Strength (MPa)	Elongation (%)
AA5754-O (Al)	76.2 x 38.1 x 3.6	102	234	21
AZ31B-H23 (Mg)	76.2 x 38.1 x 1.7	190	271.5	23.2~24.8
CFRP (PA66 with 40% carbon fiber)	76.2 x 38.1 x 3	No Data	221	1~3

3.2.2 FSBR process

FSBR experiments were conducted on a Bridge CNC machine, where the feed rate was 120 mm/min and the spindle speed was 5000 rpm. The material-stacking configurations were optimized based on preliminary research [18] to achieve best tensile performance, which were designated as FSBR Mg/CFRP, CFRP/Al, and Mg/Al joints (the first material indicated was placed on the top). The clamping region was 38.1mm x 38.1mm.

3.2.3 Tensile and acoustic emission tests

The quasi-static tensile tests were conducted at a crosshead displacement rate of 3 mm/min in metal rolling direction on an Instron 5500R universal testing machine. Clamped length was 25 mm. Two spacers were required to align the joint at the clamping areas. A single channel AE system (MISTRAS Group, Princeton Junction), including a transducer (Wsa, 100-1000 KHz) and AEwin® software, was applied to record acoustic events during the tensile tests. The

transducer was taped near the joint on the Al workpiece for as-fabricated FSBR Mg/Al and CFRP/Al joints, and on the CFRP workpiece for CFRP/Mg joints.

3.2.4 Fractographic analysis

For the fractured microstructure analysis, scanning electron microscopy (SEM) was performed. For this purpose, the fractured surfaces of tested joints were coated with a layer of 12nm thick conductive carbon layer to inhibit charging and improve the electron signal required for topographic examinations. SEM machine used was JEOL JXA-8500F electron probe micro analyzer with an image resolution of 3.0 nm.

3.3 Fractographic analysis of failure mode

The failure modes with their fractographic characteristics of dissimilar FSBR joints with three different material combinations are discussed in this section. The three configurations are Mg/CFRP, CFRP/Al, and Mg/Al selected for this study.

Different failure modes observed for the FSBR joints include tension, shearing, cleavage, pull-out; bearing followed by cleavage, and mixed failure (i.e., tension with shearing). Detailed characteristics of these failure modes are given in Appendix A.

3.3.1 Failure modes description of FSBR Mg/CFRP joints

From experiments, it was found that the failure occurs either at CFRP (tension failure) or Mg side (mixed failure of tension and shearing). In addition, the rivet pullout was also observed. These three failure modes are presented in Figs. 3.1 (a-c). Out of the total 10 samples tested, 05 samples failed in tension mode, while 03 and 02 samples failed in mixed and rivet pullout mode.

For tensile failure sample, the rivet is not pulled out from the joint; and both Mg and CFRP have secondary bending. For pull-out failure mode, the rivet is totally pulled out and the bending deformation of Mg sheet is larger than the Mg sheet of tensile failure sample. The mixed failure mode is introduced by partially pulled out rivet. The partially pull-out rivet rotates in CFRP sheet

due to the changing of force condition; therefore, the tensile loading on CFRP sheet decreased (by timing a sinθ) and the bending deformation of CFRP is very small. A detail of secondary bending phenomenon is given in Appendix B. These are the reasons that CFRP does not fail in mixed failure mode sample. However, Mg sheet has a larger bending moment and deformation under this condition. Because of the non-regular secondary bending, the edge of rivet head compresses on Mg workpiece during the tensile test which applies an extra force on Mg sheet, as indicated in the circled region in Fig. 3.1 (c).

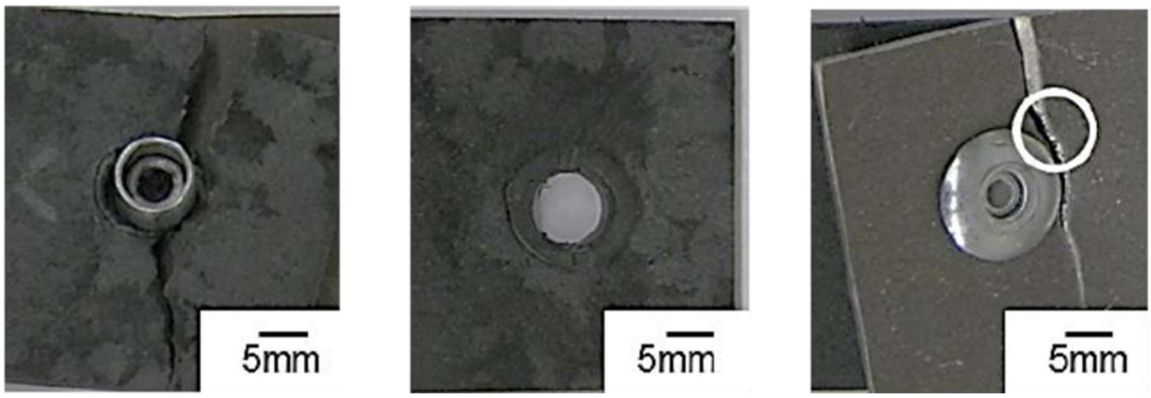

(a) (b) (c)

Figure 3.1 Failure modes of Mg/CFRP as-fabricated joints: (a) tension (CFRP fractured), (b) pull-out, and (c) mixed failure with tension and shearing (Mg fractured), where the circled region indicating the compression on Mg workpiece introduced by the edge of rivet head.

The complex failure modes in this joint are likely because of the absence of interlocking bond between the two materials (more detailed discussion on interlocking will be given in sections 3.3.2 and 3.3.3). For CFRP, tensile failure occurs caused by the presence of fiber fracture and pullout. For Mg material, mixed mode of failure happens. This is evident form SEM analysis of the specimen shown in Fig. 3.2, which presents rough tensile fracture surfaces and shearing bands.

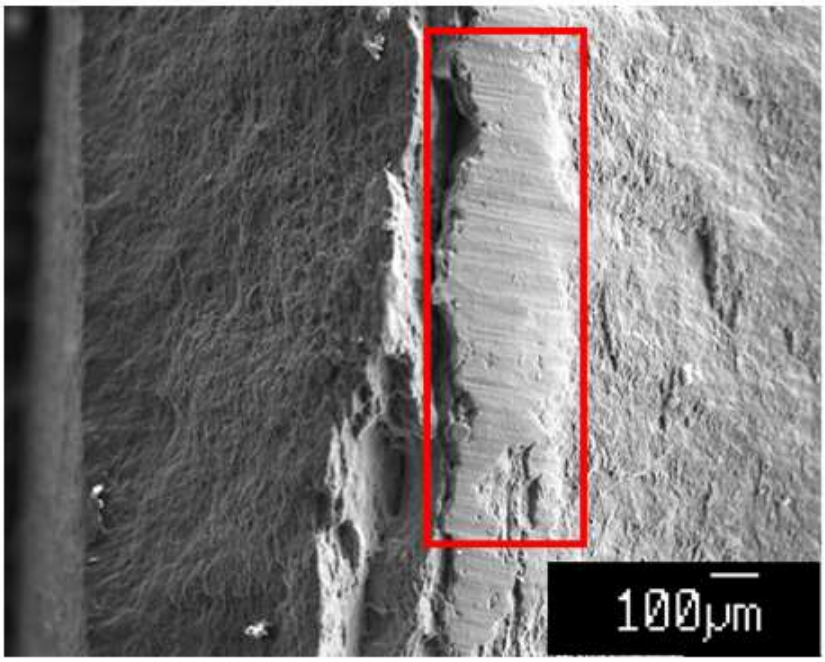

Figure 3.2 SEM Mg fracture surface of mixed failure, where the rough surfaces and circled region indicating tensile and shearing fracture characteristics, respectively.

3.3.2 Failure modes description of FSBR CFRP/Al joints

Two types of failure modes were found in FSBR CFRP/Al joints; tension mode and cleavage failures in CFRP. However, percentage of joints failing in cleavage mode is very small compared to tension failure joints. A total of 13 joints were tested out of which only 01 failed in cleavage mode. The failure modes of as-fabricated CFRP/Al FSBR joints are presented in Figs. 3.3 (a) and (b) for tension and cleavage failures in CFRP workpieces, respectively. The presence of mechanical interlock (indicated in Fig. 3.4), which provides additional interfacial bonding between the two, thus preventing form slippage or shearing of rivet; and leads to the majority failure in tension.

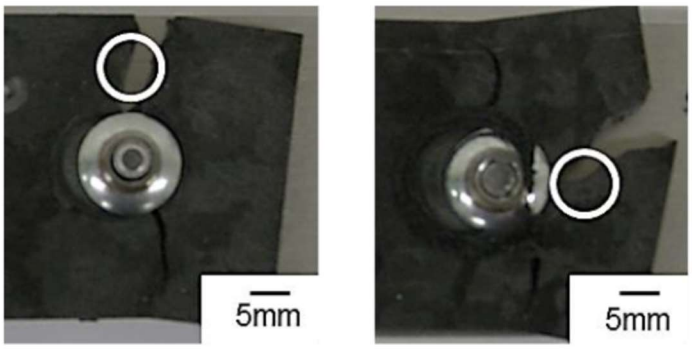

(a) (b)

Figure 3.3 Failure modes of as-fabricated CFRP/Al joints: (a) tension and (b) cleavage. Circled regions were further analyzed for SEM and results are shown in Figs. 3.5 (a) and (b).

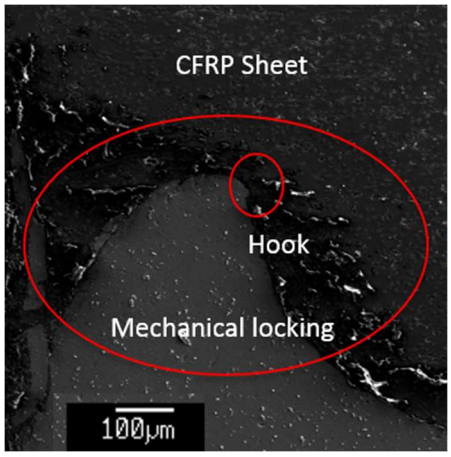

Figure 3.4 The mechanical locking in CFRP/Al joint

Figures 3.5 (a-b) describe the fracture surfaces of CFRP corresponding to the failure modes in Figs. 3.3 (a-b). In tension failure of as-fabricated joints (Fig. 3.5 a), the carbon fibers protrude in random directions and the fracture surface of the matrix is relatively rough compared to the cleavage failure case. At the cleavage facture surface (Fig. 3.5 b), the carbon fibers extrude from the nylon matrix and aligned in the similar direction (white arrow). This is because the fibers were located in the stir zone and rearranged in tangential to the rotation direction during the friction stir process [19].

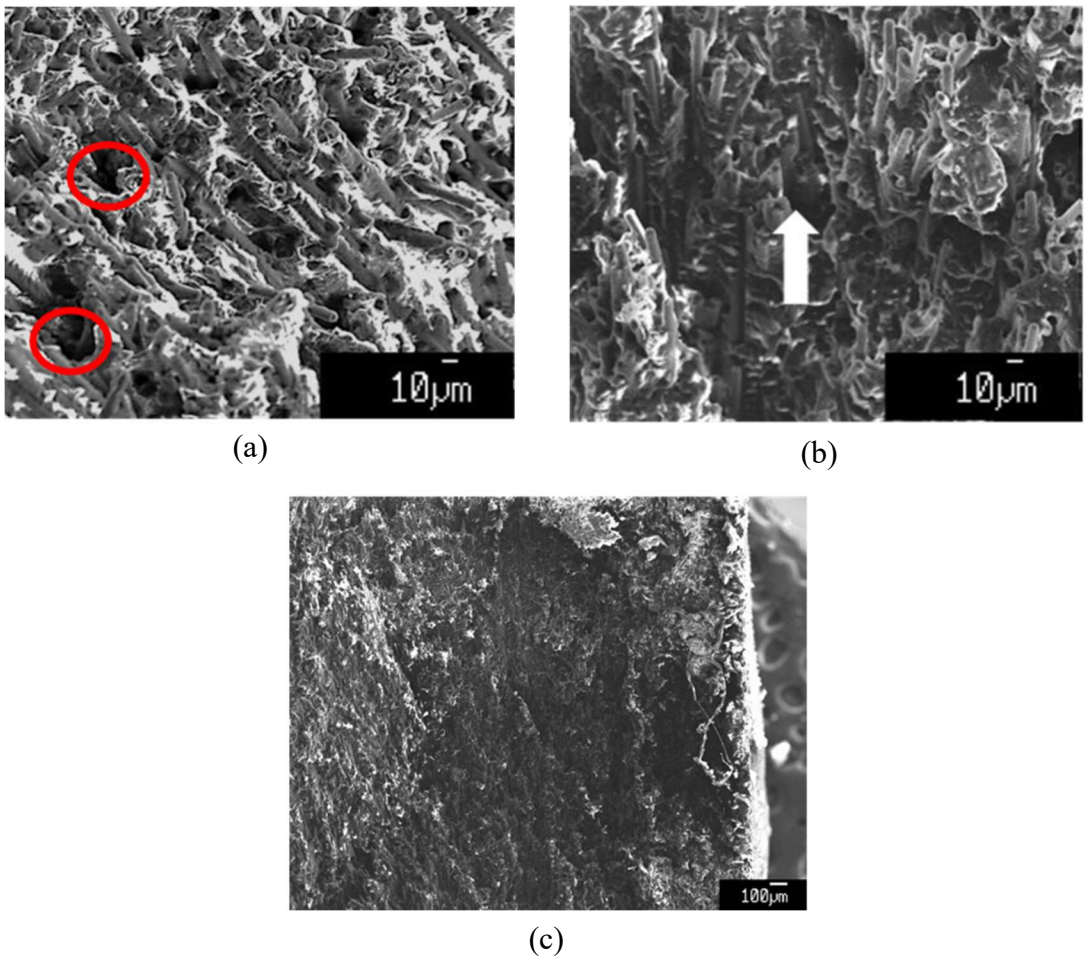

(a) (b)

(c)

Figure 3.5 SEM fracture surfaces of CFRP in as-fabricated joints: (a) tension failure circled region showing fiber pullout failure; (b) cleavage failure, arrow showing direction of fractured fibers; and (c) crushed fibers in CFRP.

Figure 3.5 (a) reveals a large number of fractured fibers along with presence of some fibers pull-outs. The dark circled regions in the micrograph indicate the regions of fiber pullout which left a hole in the matrix. However, occurrences of fiber fractures are more compared to fiber pull-outs. Fiber pull out is found throughout the fractured surface. The pullout lengths are found to be minimal and hence, they exhibit more or less uniform fracture. Therefore, failure in tension test is primarily due to fiber fracture rather than fiber pullout. The fibers fracture direction is also found to be random. Moreover, a significant area of Fig. 3.5 (b) shows brittle failure of individual fibers. These fiber fractures prove that the interfacial bonding between fibers and matrix is strong enough and fracture is caused by fiber breakage rather than debonding between

the fibers and the matrix. Other fractographic features such as crushed fibers and resin fragments are also observed, as indicated in Fig. 3.5 (c).

In tension failure mode, a microscopic crack or porosity, due to friction stir or blind riveting process [19], acts as a stress concentrator for transverse propagation of crack. The broken fibers bundle in that area is responsible for the crack initiation. After initiation, the crack tends to grow and displays an almost uniform fracture surface. Because of good interfacial bonding between fiber and matrix, with subsequent loading, the crack tends to propagate into the matrix. With further increase in load, crack further propagates through successive adjacent regions of the constituent elements (fibers and matrix). An unstable fracture occurs when the net load carrying capacity of the composite reduced to that of the applied load. The step in final fracture is a successive fracture without bridging.

It is found from literature [20] that longitudinal fracture occurs whenever the shear stress, τ_m, in the matrix extents to the ultimate shear stress, τ_{mu}. This originates longitudinal splitting which is primarily due to longitudinal fracture of matrix or debonding process. In the current research, the CFRP composite exhibit good interfacial bonding. As a result, the ultimate shear stress of the matrix, τ_{mu} is less than the debonding stress τ_d. Consequently, longitudinal fracture of matrix occurs in preference to debonding and leads to the cleavage failure.

3.3.3 Failure modes description of FSBR Mg/Al joints

Three different failure modes (Figs. 3.6 a-c) are observed for as-fabricated FSBR Mg/Al joints, which are tension, shearing, and bearing followed by cleavage. However, the dominant mode of failure is tension mode. Out of the total 11 samples tested, 67% samples failed in tension mode, while only 16% failed in shearing and bearing mode.

Most probable cause of high rate of tension mode failure is presence of mechanical interlocking between the two material sheets after FSBR process (Fig. 3.7). The interlocking helps in forming a strong bond between the two metals. Therefore, only few samples failed because of shearing or cleavage failure. Failure of all the tested specimens occurred at Mg workpiece, which is primarily because Mg sheet is thinner as compared to Al workpiece.

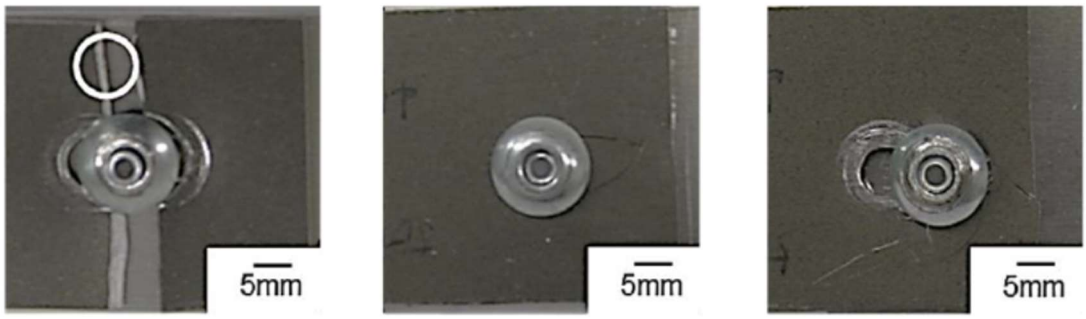

(a) (b) (c)

Figure 3.6 Different failure modes in as-fabricated FSBR Mg/Al joints: (a) tension, (b) shearing, and (c) bearing followed by cleavage.

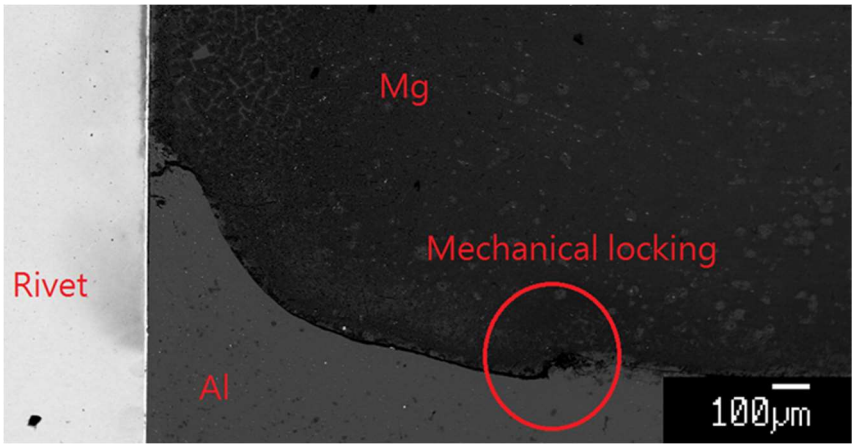

Figure 3.7 Mechanical locking at the interface of Mg and Al sheets

The fracture surfaces of the tensile test specimens were characterized by SEM, and fracture morphology is shown in Fig. 3.8. Presence of dimples and tearing ridges are observed throughout the fractured surface, as indicated by the circles. This fact directs that the failure has a mixed fracture feature of cleavage and dimples.

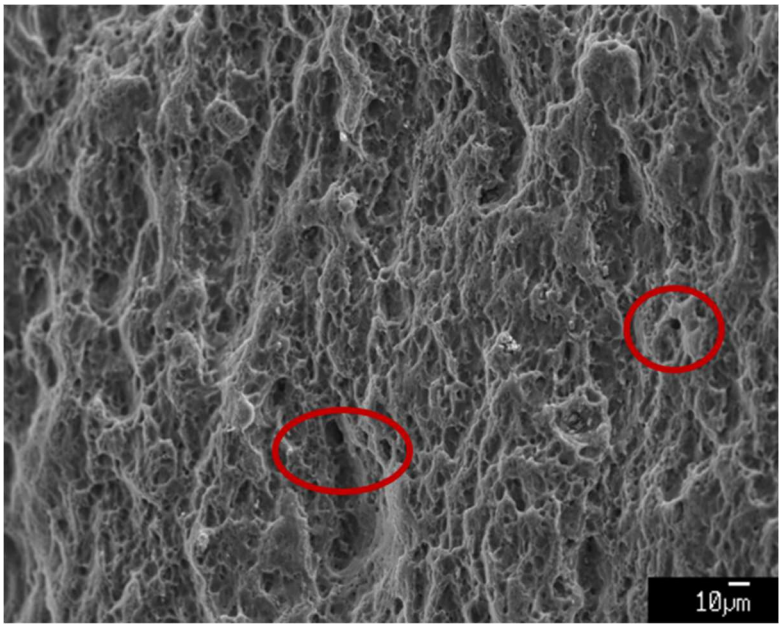

Figure 3.8 SEM fracture surfaces: circled regions highlighting characteristic dimple caused by ductile failure

3.4 Acoustic emission analysis of failure mode

AE analysis was performed with an aim to detect the damage propagation prior to the development of ultimate failure. The failure modes in lap shear joints are identified by using different AE parameters such as cumulative counts and amplitude. The damage signals were identified by the sequence of events in the tensile deformation. Details for each dissimilar FSBR joints with three different material combinations are discussed in this section.

3.4.1 Characterization of failure modes of FSBR Mg/CFRP joints

Three failure modes are observed in as-fabricated FSBR Mg/CFRP joints, which are tension failure of CFRP, rivet pullout, and mixed failure of Mg, where are presented in Figs. 3.9 (a), (b) and (c), respectively.

Acoustic emission starts after the initiation of local plastic deformation, and AE counts increase steeply up to failure. Figure 3.9 (a) represents the AE response of tensile failure mode of

CFRP. It can be seen from the figure that initially there are few AE signal responses. This AE signal continues till the middle of Zone II (plastic deformation). This may be because initially the deformation is taking place in Mg along with some micro cracking in the nylon matrix. From the FE analysis of the Mg/CFRP joint (Appendix Figs. D1 and D2), it is found that the total effective plastic strain in the Mg sheet is much smaller as compared to the strain in CFRP sheet. Thus, major portion of the displacement takes place in CFRP. According to AE analysis, deformation of Mg/CFRP joint can be divided in three zones. Zone I: elastic deformation; Zone II: plastic deformation after a threshold extension value; and Zone III: instable deformation. This distribution is in a good agreement to the mechanical response (load-extension curve) of the joint.

In case of rivet pull out failure mode (Fig. 3.9 b), there is only one hit observed in Zone II. This is because there is no significant cracking/ deformation on either CFRP or Mg workpiece. The only signal was from when the joint failed because of rivet pullout.

For the third case, mixed failure of tension and shear in magnesium, only a single rise is noticed in the hits curve (Fig. 3.9 c) in Zone II. However, the threshold extension value is greater than the rest of two failure modes. The Zone III is related to the unstable fracture region. Here the total number of hits is more than 100 hits. This is mainly because the AE receives more signals when the Mg fails than CFRP. In addition, since the AE signals depends upon the orientation and depth with which they are interacting with the flaw, greater cumulative counts are generated in case of tensile failure. In shear failure mode, acoustic emissions are striking randomly to the failure progression path. This is one reason for the less cumulative hit counts in shear failure as compared to the tensile failure mode. The same feature is mentioned in Ref [21]. Another possible reason for more AE counts is the generation of more cracks or damage accumulation in tensile failure as compared to shear failure mode. From the AE signal data, it can be concluded that in case of mixed failure mode of Mg, shear failure occurred first followed by tensile failure.

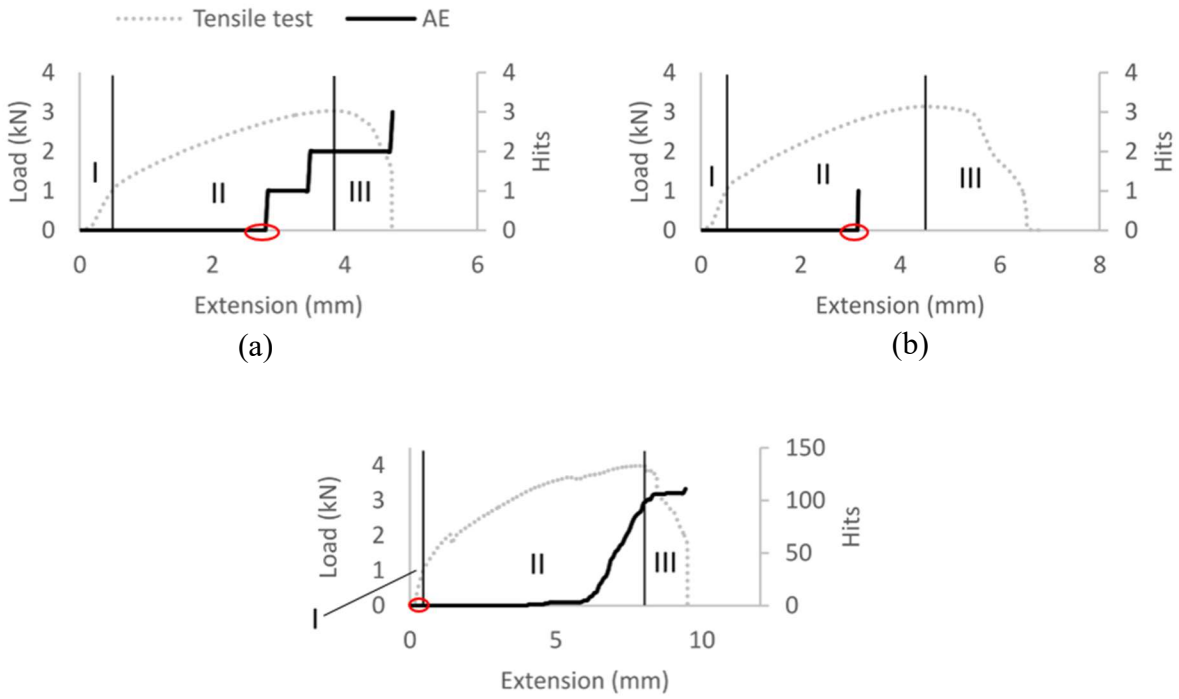

Figure 3.9 Load-extension and accumulative hit curves of as-fabricated Mg/CFRP joints, where AE sensor was placed on CFRP: (a) tension failure (CFRP fractured), (b) rivet pullout failure, and (c) mixed failure of tension and shearing (Mg fractured). Circles showing the threshold extension.

Therefore, from damage accumulation profile in terms of AE, three well-defined stages of mechanical behavior were distinguished: a linear stage (reversible response or elastic deformation) which can be characterized by a threshold value, an irreversible plastic deformation, and lastly, coalescence of damage together with localized micro-cracking growth processes including fiber fracture resulting in failure.

3.4.2 Characterization of failure modes of FSBR CFRP/Al joints

The damage signals were identified by the sequence of events in the deformation. These modes include aluminum deformation and failure of CFRP (including matrix micro cracking, matrix macro cracking, fiber pull out and fracture of fibers [23]). It is imperative to mention that

the only difference between micro- and macro-cracking in the CFRP matrix is of the saturation, i.e. a diffuse coalescence, and of the former brings to the generation of the latter.

Figures 3.10 (a) and (b) depict the responses of two different fracture modes (tensile and cleavage failure) of CFRP/Al specimens which exhibit two different fracture loads levels in terms of AE cumulative counts. From the FE Analysis of the Mg/CFRP joint, it was found that the effective plastic strain in the Mg plate is much smaller than the strain in CFRP sheet. In addition, the Al has a comparable low elongation and slightly lower strength but is thicker compared to Mg (Table 3.1). Therefore, it can be safely assumed that the final effective plastic strain of Al when the joint failed is less than CFRP as well. Consequently, the major failure of CFRP/Al joints is because of damage accumulation in CFRP. Hence, for the current analysis, different failure modes of the CFRP are analyzed as majority of the AE signals generated from the CFRP, which agrees with previous research [22]. This is further confirmed from the visual observation of that fracture (i.e. tension and cleavage) also took place in CFRP. For these two failure modes, the entire mechanism can be divided into three stages based on cumulative counts (as seen in Fig. 3.10). From Figs. 3.10 (a) and (b), it can be seen that the cleavage failure lead to a larger extension (11mm) compared to the tension failure (5.6mm). This is because of the longer bearing period (i.e. the region before the hits curve rises up in Zone II). It is imperative to note that the cumulative counts are much larger in the case of tensile CFRP failure for CFRP/Al joints as compared to the Mg/CFRP joints. This is mainly because that AE was placed on the Al for CFRP/Al joint but on CFRP for Mg/CFRP; and metal usually receives more AE signals than CFRP composite.

The first stage is characterized by macroscopic linear behavior for this type of joint with very limited elastic extension and consequently strain. In both types of failure mechanisms, the threshold extension (shown by circled region), for the onset of AE activity, is a very small proportion of the total strain or deformation. It can therefore be inferred from the AE finding that there exists a threshold below which no damage is initiated, which is mainly the elastic deformation. Comparing the damage accumulation in two failure modes, it can be seen that there is a more abrupt rise in stage II for tensile failure mode as compared to the cleavage failure mode. The same trend is demonstrated in stage III as well.

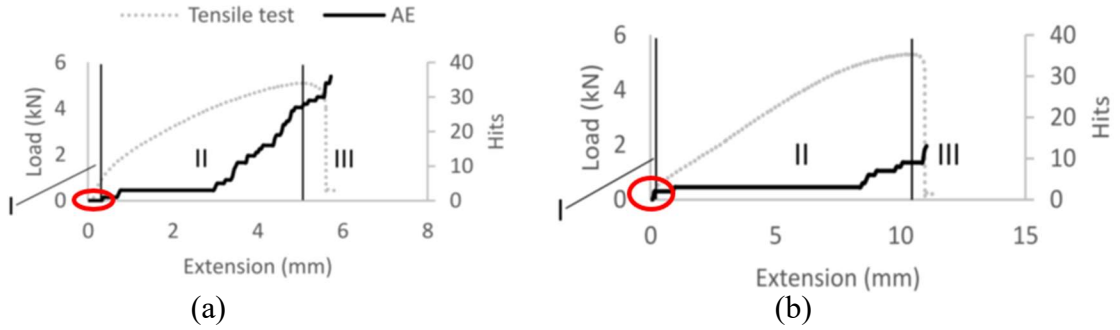

Figure 3.10 Load-extension and accumulative hit curves of as-fabricated CFRP/Al FSBR joints, where AE sensor was placed on Al: (a) tension failure, and (b) cleavage failure, where the circled region showing threshold extension.

Based on the AE analysis, it is deduced that initially there was slight matrix micro-cracking in the joint [21]. This was represented by almost flat relationship (Stage II) between cumulative AE counts vs. extension. Further loading results in progression of matrix micro-cracking at a faster rate. This resulted in a sudden increase in AE cumulative count. The final sharp increase in the count rate is deemed representing fiber pull out, fiber failure and matrix macro-cracking, which lead to the final fracture of the CFRP composite.

3.4.3 Characterization of failure modes of FSBR Mg/Al joints

Figures 3.11 (a-c) present the tensile load-extension and AE accumulative hit curves of as-fabricated FSBR Mg/Al joints, where the AE sensor was placed on the Al side. There are three failure modes characterized in Mg/Al joints. They are tension, shearing and bearing followed by cleavage failure modes. As indicated by the load-extension curves, both tension (Fig. 3.11 a) and shearing failure (Fig. 3.11 b) joints have three peaks. However, in bearing followed by cleavage failure mode (Fig. 3.11 c), multiple peaks are observed. This is primarily because Mg debris was peeled off by the interaction with the rivet body during the bearing process. The debris then was clamped between the rivet and Mg workpiece resulting in multiple AE signals [23]. Four deformation zones are identified based on tensile load-extension curves. Zone I is linear elastic deformation (reversible) prior to non-linear plastic deformation. Zone II is primary plastic deformation, starting from the end of Zone I to the maximum load. Zone III is secondary plastic

deformation, which is from the maximum load to the second maximum peak in the load curve. Lastly, Zone IV is unstable deformation, where the joint starts to lose stability and develop the failure under lap-shear tension.

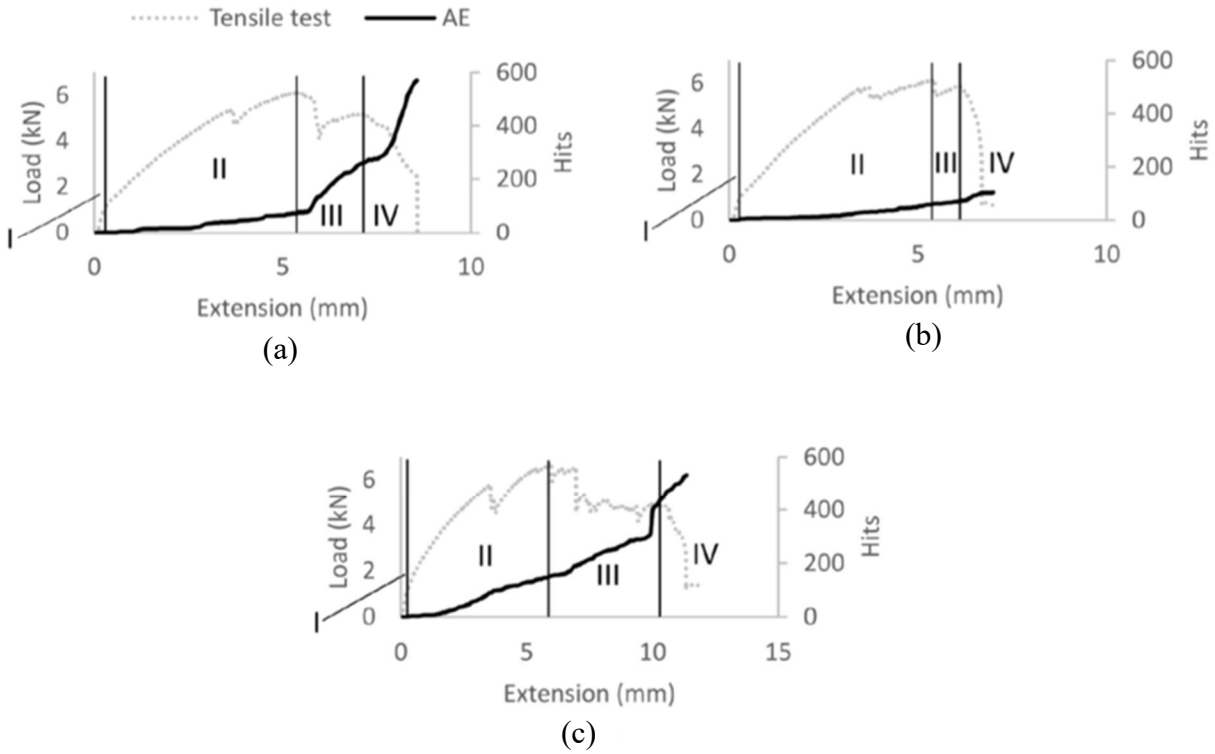

Figure 3.11 Load-extension and accumulative hit curves of as-fabricated FSBR Mg/Al joints, where AE sensor was placed on Al: (a) tension failure, (b) shearing failure, and (c) bearing followed by cleavage failure.

The AE cumulative hit curves plotted in Figs. 3.11 (a-c) indicate that there are few hits in Zone I for all three failure modes (i.e. tension, shearing and bearing followed by cleavage), which is mainly because of the recoverable elastic deformation. Referring to Fig. 3.11 (a), the tension failure joints have three increased slopes in the accumulative hit curve for Zone II, Zone III, and Zone IV. The main reason is that during both Zone III and Zone IV, Mg encountered one major cracking on the each side of the rivet successively during deformation. For a shearing failure joint (Fig. 3.11 b), there are no significant slope changes of AE hit curve in Zone II and

Zone III; and the slope increases slightly in Zone IV. The bearing followed by cleavage failure joint (Fig. 3.11 c) shows a sudden increase in the slope of AE accumulative hit curve at the end of Zone III, which indicates the occurrence of cleavage cracking in Mg workpiece. For these three cases, the first peak (the one prior to maximum peak) in the load curve is caused by slightly bearing when the rivet body compressed Mg workpiece, which, however, has no significant influence on the slope of cumulative hit curve.

3.5 Conclusions

Combined in situ acoustic emission (AE) and lap-shear tensile testing was performed on the FSBR joints, which provided meaningful information to identify the defect formation and failure modes. The AE accumulative hit history curve was found to be an efficient method to discriminate the deformation characteristics such as deformation zone and failure mode, which could not be observed with traditional extensometer measurement method. From the AE parametric analysis data, different dominate failure zones for each type of joint were predicted. The different shapes of AE signals in plastic deformation (i.e. Zone II of Mg/CFRP and CFRP/Al joints, and Zone II and Zone III of FSBR Mg/Al joints) facilitate the characterization of tensile behavior.

In general, from damage accumulation profile in terms of AE, three well-defined stages of mechanical behavior was distinguished: linear stage (reversible response or elastic deformation) which can be characterized by a threshold value, this is followed by commencement of irreversible deformation. Lastly, coalescence of damage together with localized micro-cracking growth processes results in failure. The slope of AE curve increases significantly in the middle of Zone II, which is related to the extension of the hole left by the rivet. Furthermore, the failure mode with fracture surface perpendicular to loading (i.e. tensile failure) has higher hit counts than the failure mode with the fracture surface parallel to loading (i.e. shear or cleavage failure). The transition from Zone II to Zone III is separated by the significant localized jump at the cumulative AE counts. Comparison with the load extension curve reveals that the abrupt increase in the AE counts is accompanied by a deviation from linearity in the load–extension curve.

Different combinations of joints (w.r.t materials) exhibit distinct failure modes. For as-fabricated CFRP/Al FSBR joints, tension and cleavage failures occurred in CFRP workpiece. In tension failure mode, the main cause of failure is primarily due to fiber fracture rather than fiber pullout. These fiber fractures prove that the interfacial bonding between fibers and matrix is strong enough and fracture is caused by fiber breakage rather than debonding between the fibers and the matrix. Other fractographic features such as crushed fibers and resin fragments are also observed. In cleavage failure mode, longitudinal fracture of matrix occurs in preference to debonding.

Three different failure modes were observed for as-fabricated FSBR Mg/Al joints, which are tension, shearing and bearing followed by cleavage. However, the dominant mode of failure is tension mode. Presence of dimples and tearing ridges are observed throughout the fractured surface. This phenomenon indicates that the failure has a mixed fracture feature of cleavage and dimples

In as-fabricated FSBR CFRP / Mg joints, it was found that the failure occurred either at CFRP (tension failure) or Mg side (mixed failure of tension and shearing). In addition, the rivet pullout was also observed. For CFRP, tensile failure occurs caused by the presence of fibers in the longitudinal direction. For Mg material, mixed mode of failure happens which presents rough tensile fracture surfaces and shearing bands. The different failure modes are related to the microstructural characteristics generated by FSBR process, for example the formation of mechanical interlocking.

REFERENCES

[1] D. Gao, U. Ersoy, R. Stevenson and P.-C. Wang, 2009, "A new one-sided joining process for aluminum alloys," ASME Journal of Manufacturing Science and Engineering, 131(6), pp.

[2] J. Min, J. Li, Y. Li, B. E. Carlson, J. Lin and W.-M. Wang, 2015, "Friction stir blind riveting for aluminum alloy sheets," Journal of Materials Processing Technology, 215, pp. 20-29.

[3] J. Min, J. Li, Y. Li, B. E. Carlson and J. Lin, 2014, "Mechanical property of Al alloy joints by friction stir blind riveting," Procedia Engineering, 81, pp. 2036-2041.

[4] J. Min, Y. Li, J. Li, B. E. Carlson and J. Lin, 2015, "Mechanics in frictional penetration with a blind rivet," Journal of Materials Processing Technology, 222, pp. 268-279.

[5] J. Min, J. Li, B. E. Carlson, Y. Li, J. F. Quinn, J. Lin and W.-M. Wang, 2015, "Friction stir blind riveting for dissimilar cast Mg AM60 and Al alloy sheets," ASME Journal of Manufacturing Science and Engineering, 137(5), pp.

[6] G. L. Kulak, J. W. Fisher and J. H. Struik, 1987, Guide to design criteria for bolted and riveted joints, Wiley, New York.

[7] S. D. Thoppul, J. Finegan and R. F. Gibson, 2009, "Mechanics of mechanically fastened joints in polymer–matrix composite structures – A review," Composites Science and Technology, 69(3-4), pp. 301-329.

[8] S. Heimbs, S. Schmeer, J. Blaurock and S. Steeger, 2013, "Static and dynamic failure behaviour of bolted joints in carbon fibre composites," Composites Part A: Applied Science and Manufacturing, 47, pp. 91-101.

[9] J. Ekh, J. Schön and L. Gunnar Melin, 2005, "Secondary bending in multi fastener, composite-to-aluminium single shear lap joints," Composites Part B: Engineering, 36, pp. 195-208.

[10] M. Skorupa, A. Korbel, A. Skorupa and T. Machniewicz, 2015, "Observations and analyses of secondary bending for riveted lap joints," International Journal of Fatigue, 72, pp. 1-10.

[11] Á. Olmedo and C. Santiuste, 2012, "On the prediction of bolted single-lap composite joints," Composite Structures, 94, pp. 2110-2117.

[12] S. Masmoudi, A. El Mahi and R. El Guerjouma, 2014, "Mechanical behaviour and health monitoring by acoustic emission of sandwich composite integrated by piezoelectric implant," Composites Part B: Engineering, 67, pp. 76-83.

[13] P. F. Liu, J. K. Chu, Y. L. Liu and J. Y. Zheng, 2012, "A study on the failure mechanisms of carbon fiber/epoxy composite laminates using acoustic emission," Materials and Design, 37, pp. 228-235.

[14] M. Kempf, O. Skrabala and V. Altstädt, 2014, "Reprint of: Acoustic emission analysis for characterisation of damage mechanisms in fibre reinforced thermosetting polyurethane and epoxy," Composites Part B: Engineering, 65, pp. 117-123.

[15] A. Marec, J. -H. Thomas and R. El Guerjouma, 2008, "Damage characterization of polymer-based composite materials: Multivariable analysis and wavelet transform for clustering acoustic emission data," Mechanical Systems and Signal Processing, 22(6), pp. 1441-1464.

[16] N. Godin, S. Huguet, R. Gaertner and L. Salmon, 2004, "Clustering of acoustic emission signals collected during tensile tests on unidirectional glass/polyester composite using supervised and unsupervised classifiers," NDT & E International, 37(4), pp. 253-264.

[17] Y. Xiao and T. Ishikawa, 2005, "Bearing strength and failure behavior of bolted composite joints (part I: Experimental investigation)," Composites Science and Technology, 65(7-8), pp. 1022-1031.

[18] W. M. Wang and J. Li, 2014, "Friction stir Blind riveting of CFRP and metals," Ph.D. qualify exam report, University of Hawaii at Manoa, Honolulu, HI.

[19] B. Croom, W.M. Wang, J. Li and X. Li, 2015, "Unveiling 3D deformations in carbon fiber reinforced polymer composites by coupled micro X-Ray computed topography and volumetric digital image correlation," Experimental Mechanics, under review.

[20] M. S. Kumar, K. Raghavendra, M. A. Venkataswamy and H. V. Ramachandra, 2012, "Fractographic analysis of tensile failures of aerospace grade composites," Materials Research, 15(6), pp. 990-997.

[21] D. Polyzos, A. Papacharalampopoulos, T. Shiotani and D. G. Aggelis, 2010, "Dependence of AE parameters on the propagation distance," in Progress in acoustic emission. Proceedings of

the 20th international acoustic emission symposium, Japanese society for non-destructive inspection (JSNDI), Kumamoto, Japan.

[22] J. Min, Y. Li, J. Li, B. E. Carlson and J. Lin, 2015, "Friction stir blind riveting of carbon fiber reinforced polymer composite and aluminum alloy sheets," The International Journal of Advanced Manufacturing Technology, 76(5), pp. 1403-1410.

[23] A. Marec, J.-H. Thomas and R. El Guerjouma, 2008, "Damage characterization of polymer-based composite materials: Multivariable analysis and wavelet transform for clustering acoustic emission data," Mechanical Systems and Signal Processing, 22(6), pp. 1441-1464.

Appendix A. Summary of failure modes and AE signal characteristics of FSBR joints

Materials	Failure Modes	Figures	Characteristics of AE hits curves
Mg/CFRP	Tension (CFRP failed)	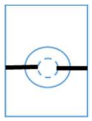	The hits curve rises up in the middle of Zone II with limited hits.
	Pull-out		Only one hit was observed in Zone II.
	Mixed (tension, shearing) (Mg failed)		The hits curve rises up in Zone II; cumulative hit counts are higher than 100.
CFRP/Al	Tension (CFRP failed)	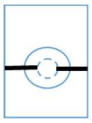	The number of hits increases in the middle of Zone II.
	Cleavage (CFRP failed)	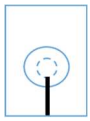	The number of hits slightly increases in the end of Zone II. Cleavage failure has lower numbers of hits than tension failure.
FSBR Mg/Al	Tension (Mg failed)	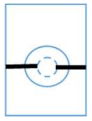	Crack propagated perpendicular to the direction of loading. Few hits occurred

			in Zone I, Zone II, Zone III, and Zone IV have distinct slopes.
	Shearing (Mg failed)	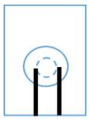	Direction of crack propagation is not perpendicular to the loading direction. Few hits were monitored in Zone I; however, no significant slope change was found in other zones.
	Bearing + Cleavage (Mg failed)	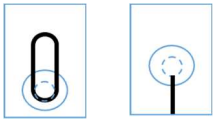	Few hits were monitored in Zone I; significant change in the slope of Zone III was observed.

Appendix B. Description of secondary bending

Secondary bending appears in all these three material combinations during tensile tests. A regular secondary bending is defined as when both top and bottom workpieces are bended (as seen in Fig. Ba). However, when CFRP workpiece is placed at the bottom, the rivet in CFRP workpiece may pull and rotate during tensile test, and only the top metal is bended. This case is defined as non-regular secondary bending (Fig. Bb). In the non-regular secondary bending, the rivet rotates a θ angle to the normal direction (dashed line in Fig. Bb); whereas the rivet remains normal to the bended workpieces in the regular secondary bending.

Analysis of the force acting on bottom CFRP, as in Fig. Bb, is directly applied to understand the increasing maximum tensile load in mixed failure mode. The acting force introduced by rivet body is F_{app}, the effective load on CFRP workpiece is given by F_{eff}, and the rivet rotates θ degrees in CFRP workpiece. If the rivet does not rotate in CFRP workpiece (Fig. Ba), the applied load from rivet body (F_{app}) is equivalent to effective load (F_{eff}) on CFRP work piece. When the

rivet rotates θ degrees in CFRP workpiece (Fig. Bb), the effective load (F_{eff}) on CFRP work piece is $F_{app} \times cos\theta$, which is less than F_{app}. Furthermore, the CFRP workpiece experiences additional bending in Fig. Ba compared to the case in Fig. Bb. Therefore, when the CFRP reaches to the failure load, the F_{app} in non-regular secondary bending is higher than the regular secondary bending, this entails a larger maximum tensile load. A vertical load $F_{app} \times sin\theta$ perpendicular to F_{eff} introduces pushing force to the CFRP workpiece and applies extra bending force to Mg workpiece. Consequently, the failure mode of Mg/CFRP FSBR joint is related to the angle θ. CFRP tensile failure occurs when θ is small; and pull-out and mixed failure (Mg failure) occur when θ is large (about 20°).

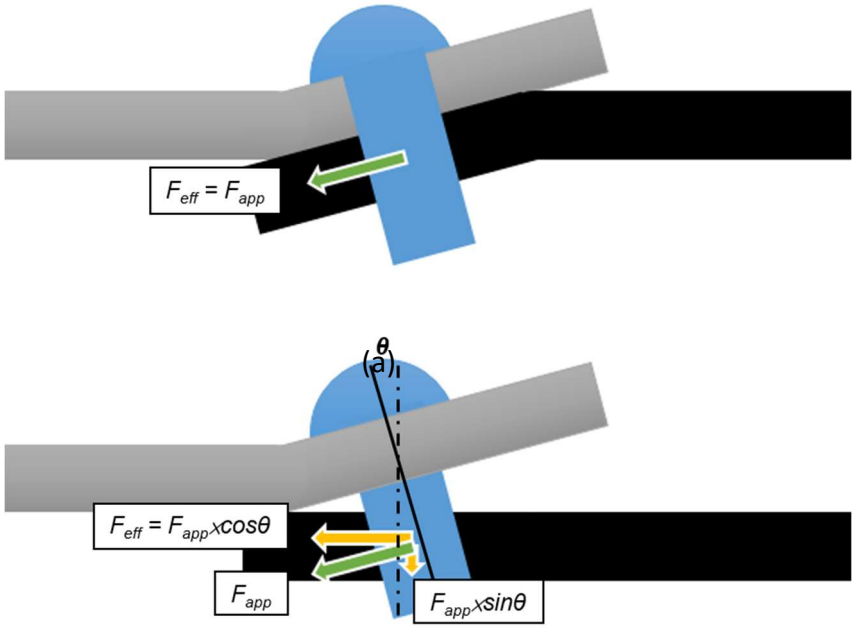

Figure B. Secondary bending of Mg/CFRP FSBR joint: (a) regular secondary bending; and (b) non-regular secondary bending (when rivet body rotates in CFRP workpiece).

Appendix C. AE amplitude plots

The AE amplitude curves are plotted to identify the joint deformation and failure mode. Examples on as-fabricated and corroded FSBR Mg/Al joints are included in Fig. C1 and Fig.C2, respectively. For a tension failure (Fig. C1a), the AE amplitude curve indicates two main peaks,

which is mainly caused by the two major cracks along both sides of rivet hole. Figure C1b illustrates that there is no significant AE peak in the shearing failure mode. The AE amplitude curve of bearing followed by cleavage failure joint has only one large peak (4098 dB), as seen in Fig. C1c, which is because of cleavage fracture. However, Fig. C1c also shows that the cleavage failure cannot be found through the load curve. Figures C2 (a) and (b) summarize the load-extension and AE amplitude curves of corroded joints at failure modes of bearing with tension and bearing with pull-out, respectively. The main difference of AE amplitude signals between these two failure modes is that more high amplitude peaks (> 1500 dB) appear in bearing followed by pull-out failure mode (Fig. C2b) than followed by tension mode (Fig. C2a).

From the above analysis, it is seen that more noisy features in the AE amplitude curve making it more difficult for diagnosis compared to accumulative hit curve.

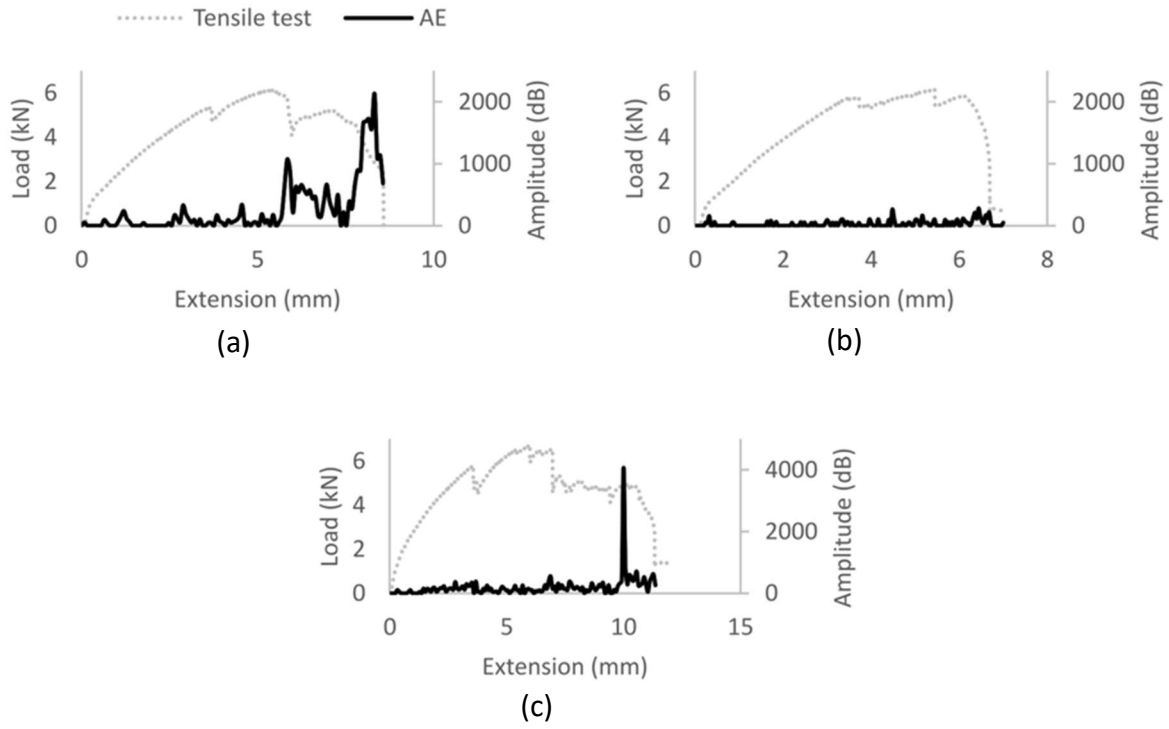

Figure C1. Load and AE amplitude curves of as-fabricated FSBR Mg/Al joints: (a) tension failure, (b) shearing failure, and (c) bearing followed by cleavage failure.

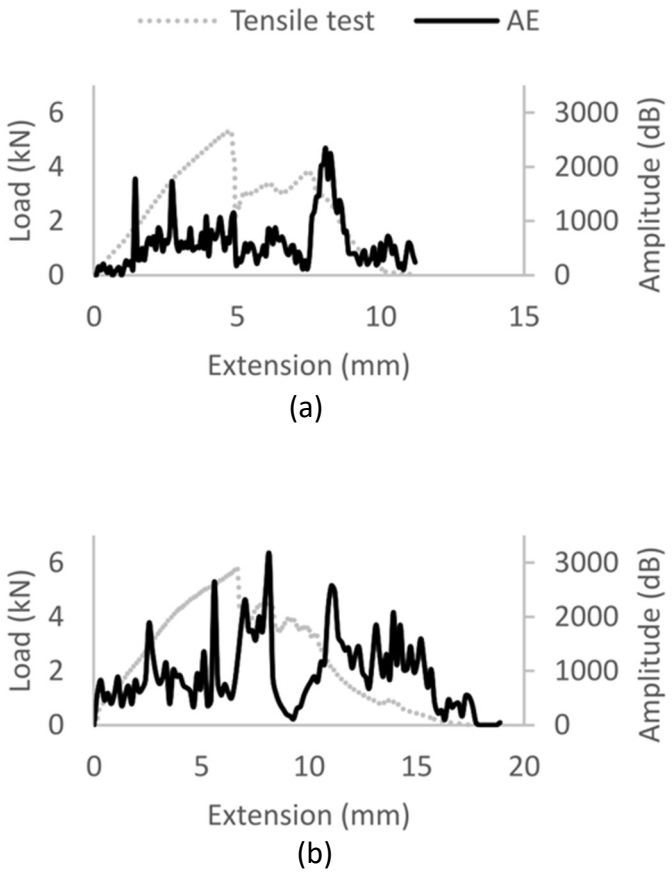

Figure C2. Load-extension and AE amplitude curves of corroded FSBR Mg/Al joints: (a) bearing followed by tension, and (b) bearing followed by pull-out.

Appendix D. FE analysis for Mg/CFRP FSBR joint

FE analysis is used to predict the failure behavior and to calculate the corresponding stresses and strains. The joint considered for the analysis is Mg/CFRP FSBR joint. Since, from the experiments it was found that any of the constituent materials can failure, thus suggesting a more complex failure mechanism. For the same reason, analysis was performed for Mg/CFRP FSBR joint. Material model 17 (oriented crack model) in LS-DYNA is selected for CFRP. This model is usually used to simulate an isotropic elastic plastic brittle material. The material model 24 (piecewise linear plasticity model) is used for Mg. The blind rivet is considered as a rigid body as its Young's modulus is much higher than Mg alloy and CFRP. Both CFRP and Mg sheets use

eight-node solid element whereas a four node tetrahedral solid element is used for rivet. Figures D1 and D2 show the effective plastic strain contour for CFRP and Mg sheets respectively.

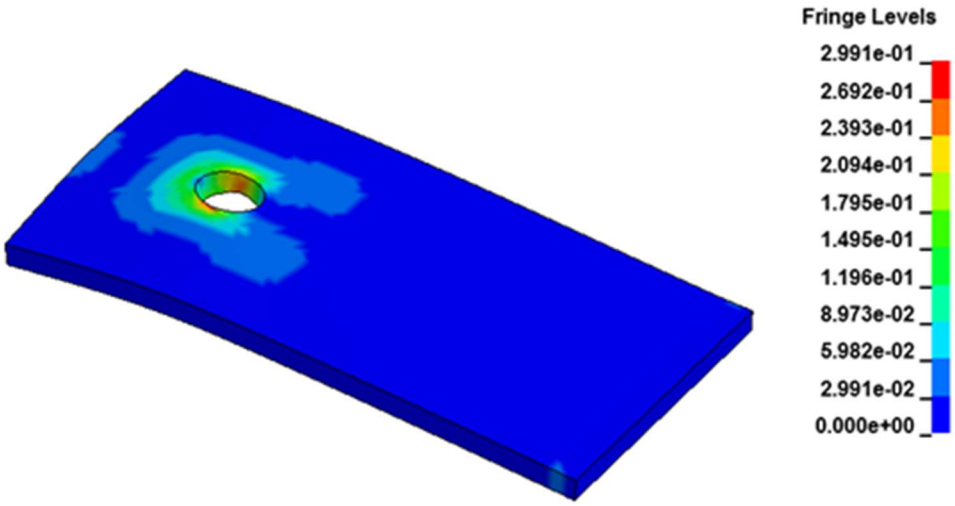

Figure D1. Effective plastic strain plot for CFRP sheet

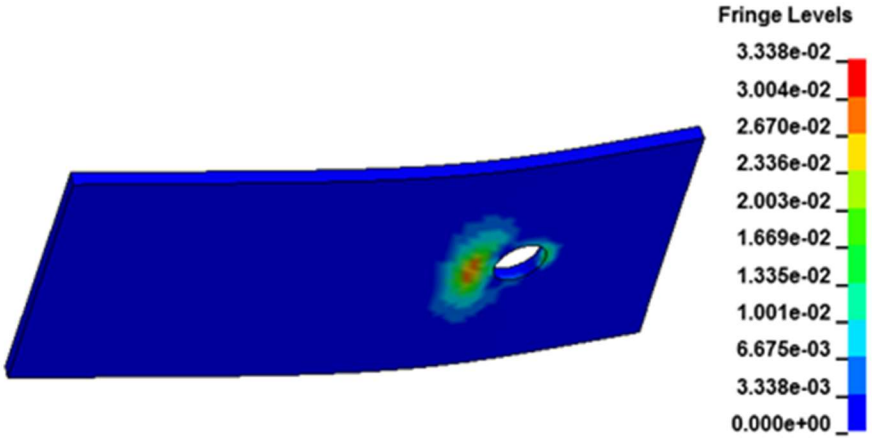

Figure D2. Effective plastic strain plot for Mg sheet

CHAPTER 4

INVESTIGATION OF THE MECHANICAL CHARACTERISTICS OF FSBR DISSIMILAR MATERIALS JOINTS EXPOSED TO MARINE ENVIRONMENT

4.1 Introduction

Currently, robustly implemented and easy to automate processes are gaining widespread attention in industries [1]. Friction stir blind riveting (FSBR) is one promising process [2] which provides high flexibility among the joining techniques. FSBR is a comparatively new high speed mechanical fastening technique used for joining similar as well as dissimilar material sheets with equal confidence [3]. FSBR is a one-sided mechanical joining technique integrating the advantages of friction stir welding, where the frictional heat generated by a rotating blind rivet softens work pieces and thus allows an easy penetration of blind rivet into work pieces under reduced force [4]. Similar to other joining technologies, FSBR also demands a comprehensive understanding of the methodology and mechanical behavior of the produced joints for its effective utilization in different industrial sectors. For this purpose, thorough research and qualification work are mandatory.

Various researchers have investigated the process parameters and mechanical properties of FSBR joints. Min and Li [5] have investigated the spindle speed and feed rate effect along with process window of Al-CFRP FSBR joints. The authors determined that parameters, such as feed rates, spindle speeds, and stack-up sequence influence the mechanical behavior of FSBR lap joints of carbon fiber reinforced polymer (CFRP) composite with aluminum alloy. Min and Li [6] explored the process windows and the influence of process parameters on joint strength of Mg - Al FSBR joints. The researchers defined FSBR process related reasons which leads to joint quality issues. Min et al. [7] also investigated the FSBR joints of Al alloy sheets. Moreover, Lathabai et al. [8] discussed the mechanical properties of different configuration of dissimilar materials sheets joined through FSBR process. Wang et al. [9] discussed the failure modes of different configurations of FSBR joints utilizing AE analysis. Li et al. [10] investigated the

atmospheric corrosion mechanisms of Al-Mg FSBR joints exposed at a severe marine test site. The authors found corrosion in the coupled region of Al in addition to the severe corrosion that occurred on Mg. The contributing mechanism in this case is the alkaline condition generated by the cathodic reaction that occurred inside of the crevice. However, no current literature examined the effect of corrosive environment on failure modes and mechanical properties of FSBR joints. Furthermore, analyzing the marine environment effects on FSBR joints becomes crucial considerations in the previous study [11] in which Srinivasan and Hihara highlighted the effect of galvanic corrosion on mechanically-coupled aluminum with carbon fiber composites. Gebhard et al. [12] focused on the effect of corrosion on combinations of different types of carbon fiber composites, where they reported the effect of type of fiber, fiber volume content and the aqueous medium on the fiber corrosion. In an investigation, Mandel et al. [13] pointed out the reasons for limited application in case of the dissimilar material joints in corrosive environmental conditions. Moreover, Bardal [14] and Calabrese [15] mentioned that the connecting of steel rivets with the aluminum sheets escalated the corrosion process owing to galvanic effects, as the two metals offer fairly different electrochemical behavior. However, no published literature is available on the variation in mechanical property responses of FSBR joints when exposed to corrosive environment.

The present work is therefore aimed at probing the effects of corrosive environment on failure modes and mechanical properties (i.e. maximum tensile load, maximum elongation to break, energy dissipated and nominal stiffness) of three configurations of dissimilar materials joints. The three materials chosen for joints include aluminum alloy (AA5754-O), magnesium alloy (AZ31B-H23) and CFRP composite, which are used widely for lightweight structures in transportation sector [16].

4.2 Experimental procedure

4.2.1 Sample preparation

The FSBR process was performed on a computer numerical control machine. The feed rate and spindle speed settings for joints manufacturing were 120mm/min and 5000rpm, respectively. The joints configurations were Mg/Al, CFRP/Al, and Mg/CFRP (the first material was on the top). Dimensions of Mg, CFRP, and Al sheets used in joints were 76.2mmx38.1mmx1.7mm, 76.2mmx38.1mmx3mm, and 76.2mmx38.1mmx3.6mm, respectively. The clamping region was 38.1mmx38.1mm. The cycle time (processing time) for the process was 30–40 s.

To understand their mechanical behavior degradation in outdoor corrosive environments, such as in the marine environment, FSBR joints were exposed to an aggressive marine atmospheric condition, Marine Corps Base Hawaii outdoor test racks, for 6 months. Joints were exposed on test racks oriented at 30-degrees from horizontal, facing northeast (towards prevailing winds), and located within 40 meters of a shoreline with waves breaking consistently. The average temperature and relative humidity were 23.6°C and 70%, respectively. Average chloride (Cl^-) deposition rates (2900mg/m^2/day) and sulfate (SO_4^{2-}) deposition rates (390mg/m^2/day) are considered extremely high, which is due to significant shore-breaking waves at the site. The Marine Corps Base Hawaii corrosion test site maintained by the Hawaii Corrosion Laboratory is located in Kaneohe, Hawaii, and is considered as a severe marine atmospheric site with regards to corrosion rates.

4.2.2 Tensile and acoustic emission testing

Instron 5500R universal testing machine was used for performing quasi-static tensile tests of exposed joints. The constant displacement rate was 3 mm/min, and the tensile direction was in metal rolling direction. The FSBR sample was clamped with two spacers at both sides, and the gauge length was 25 mm. Acoustic emission (AE) system was utilized for additional information on defect development. The transducer of AE system was taped on Al sheet for exposed FSBR Mg/Al and CFRP/Al joints, while it was placed on CFRP sheet for exposed FSBR CFRP/Mg joints due to the rough Mg surface. The single channel AE system comprised of one sensor (Wsa, 100-1000 KHz) was controlled by AEWin® software. The samples were placed at room

temperature for 1 month after receiving from site to mitigate the effect of moisture on the tensile tests results.

4.2.3 Microstructural analysis

Scanning electron microscope (SEM) analysis was conducted using JEOL JXA-8500F electron probe micro analyzer to observe fracture surface for analyzing fracture mechanism and corrosion products. To improve the imaging of samples, a carbon coating of 20nm was applied.

4.3 Results and discussion

The preceding section covers the analysis of these three configurations. Analysis of each configuration consists of two parts. The first part is detailed analysis on changes in mechanical properties (i.e. maximum tensile strength, maximum elongation to break, energy dissipated and nominal stiffness) as a result of exposure to marine environment. In the second part, microstructural analysis of the three configurations of exposed joints is presented.

4.3.1 Exposed FSBR CFRP/Al joints

4.3.1.1 Mechanical characterization

The exposed CFRP/Al joints (Figs. 4.1 a and 4.1 b) exhibit only one mode of failure, i.e. tensile failure mode in comparison to two failure modes (tensile and cleavage) of as-fabricated CFRP/Al joints investigated by Wang et al. [9]. In tensile failure mode, fracture initiated at both sides of the rivet hole and propagated perpendicular to the direction of loading; whereas in cleavage failure one fracture surface is perpendicular while the other is parallel to the direction of loading. Both the failure modes occurred due to tension loading but the cleavage failure mode is due to non-uniform tension force. It is imperative to mention that the chance of cleavage failure in as-fabricated joints is very low as compared to the tension failure mode (only one as-fabricated sample has cleavage failure and 12 samples have tensile failure out of total 13 joints tested). In the exposed CFRP/Al joints fracture took place in CFRP sheet, which is similar to as-fabricated CFRP/Al joints where the fracture also happened in CFRP sheet. In this investigation, fracture has not been observed in the aluminum sheet.

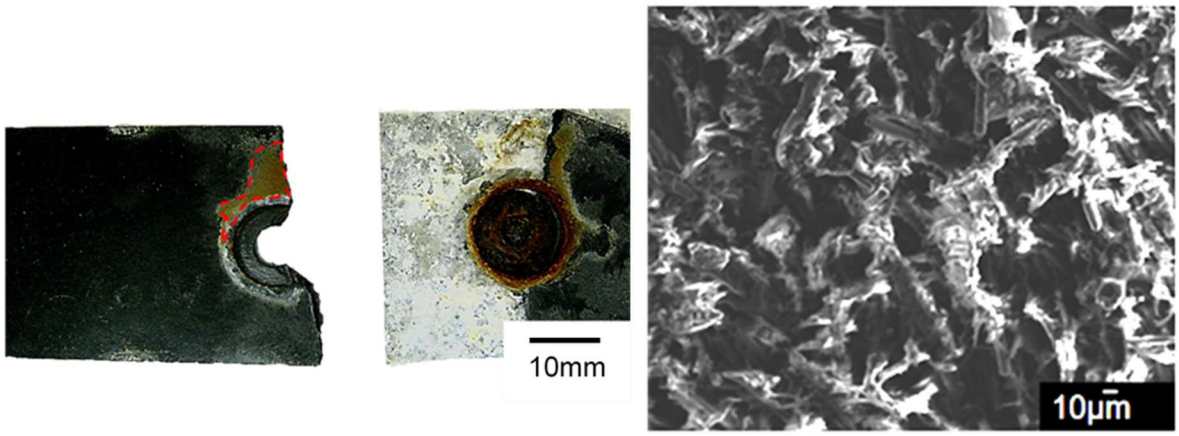

Figure 4.1 (a) Image of a fractured CFRP/Al joint in tension failure mode, and (b) an SEM image of the fractured surface of CFRP.

Figures 4.2 (a) and 4.2 (b) presents the typical load-extension and AE hit curves of the FSBR CFRP/Al joints, respectively. The maximum tensile load for exposed CFRP/Al joints ranges between 5000 to 5300 N, where CFRP fractured. The maximum tensile load is similar to the value of as-fabricated CFRP/Al joints. Another contributing factor for similar maximum tensile load values of as-fabricated and exposed joints is FSBR process itself. During the process the rivet frictionally stirred to penetrate the work materials and did not generate any gap between the rivet and the work materials, which preventsed any moisture or water content reaching at the interface area. As further visual examination of steel rivet after the tensile test (Fig. 4.2 c), it is found that the interface area between steel rivet and the sheet materials was free of corrosion. As a result, the rivet strength was considerably maintained.

From Fig. 4.2 (a), it can be seen that the “nominal stiffness” (measured from slope of the load-displacement curve) of exposed joints is lower than as-fabricated ones. The lower nominal stiffness of exposed joints is caused by the debonding between the matrix and carbon fibers in CFRP where the adhesion strength became weaker as matrix degraded. However, exposed joints exhibit larger extensions than as-fabricated joints as a result of the slippage occurred between the corroded surfaces of the overlapping sheets during the tensile test which subsequently changes the contacting and loading conditions. In addition, three zones are defined according to the load-displacement curve (similar to as-fabricated joints [9]) where Zone I is the linear elastic

deformation region, Zone II presents the non-linear deformation till maximum tensile load, and Zone III is the region after maximum tensile load until final fracture.

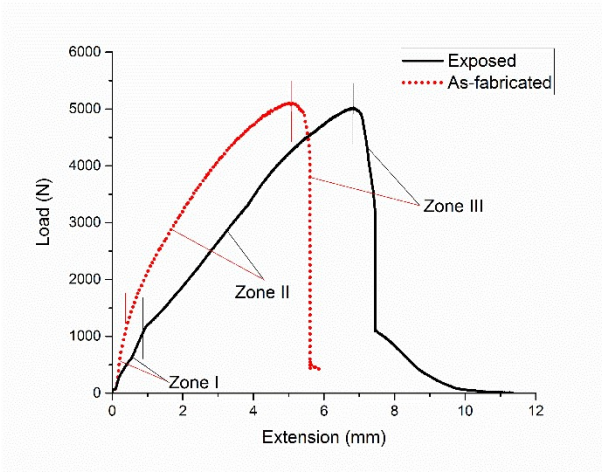

(a)

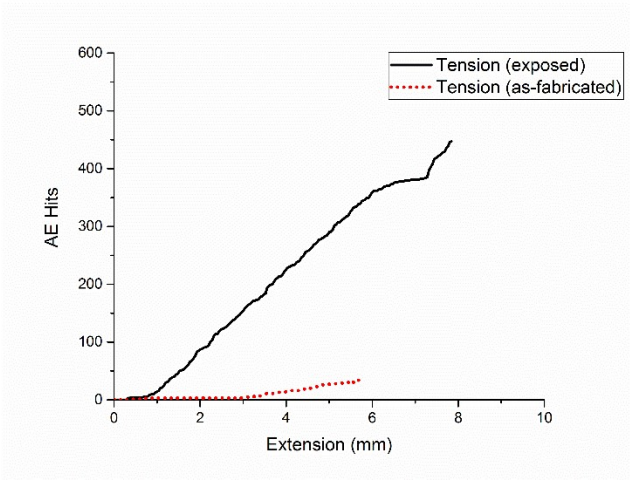

(b)

(c)

Figure 4.2 (a) Load-extension curves of the as-fabricated and corroded FSBR CFRP/Al joints with tension failure where vertical lines are demarcating different zones, (b) AE accumulative hits vs extension curves of as-fabricated and corroded FSBR CFRP/Al joints, and (c) steel rivet showing rust-free interface area in CFRP/Al exposed joints

The AE hit signals curve (Fig. 4.2 b) displays a rise in accumulative hits after the initial threshold region, which is because corrosion products was peeling out and initiation of micro-cracks in both Al and CFRP. It should be noticed that the AE sensor was placed on Al sheet during test in this case. For the exposed joints, there is a sharper increase in AE hits at the end of AE curve compared to the as-fabricated ones. This is caused by the sudden failure of nylon matrix also indicating weaker stiffness of exposed joints than as-fabricated ones. For all

CFRP/Al FSBR exposed and as-fabricated joints, AE signal hits after reaching the point of maximum tensile strength, rise again until fracture.

4.3.1.2 Microstructure

The rupture surfaces, as the microstructural morphology, is an important tool in understanding the failure mechanism, which entails a thorough comprehension of the mechanical fracture and failure properties. Microstructure analysis revealed debonding as the failure mode in exposed CFRP sheets (Fig. 4.3 a). This failure mode is absent in as-fabricated FSBR CFRP/Al joints where fiber pull out and fiber fracture are the main causes of failure (Fig. 4.3 b). However, the carbon fibers exhibit the same brittle fiber fracture mode in both types of joints (Figs. 4.3 a and b).

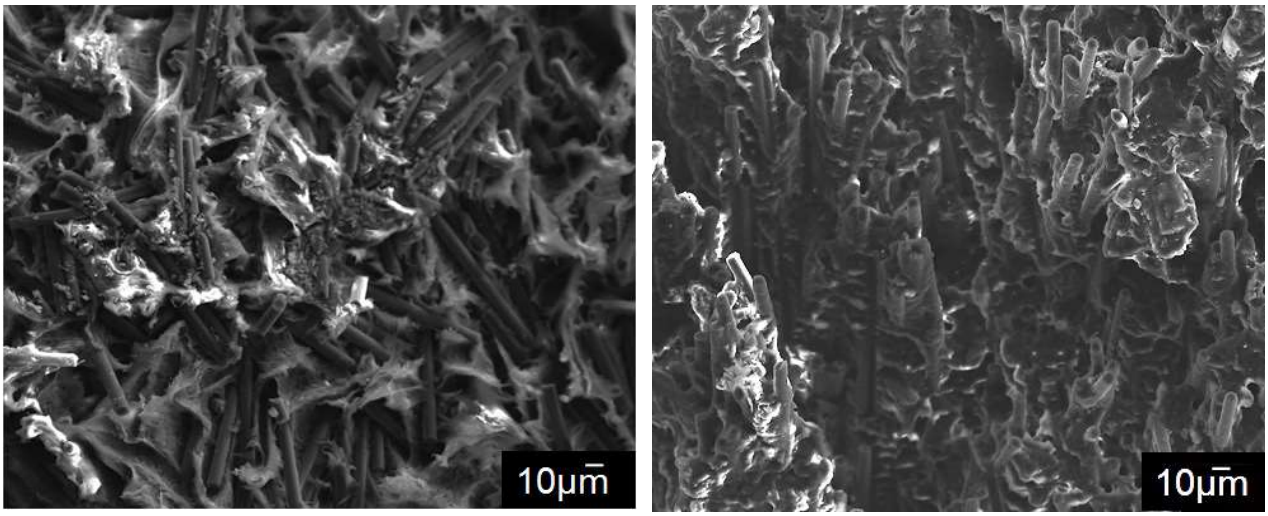

(a) (b)

Figure 4.3 SEM fracture surfaces of CFRP in exposed CFRP/ Al joints: (a) tension failure of exposed sample and bare fibers and sheared matrix are visible, and (b) tension failure of the as-fabricated sample, where fiber fracture and pull out are dominant

Moisture uptake is an important concern for the hydrophilic Nylon 66. In the present study, debonding (separation of Nylon 66 from carbon fibers) is observed in CFRP sheet which was initiated from the mechanical degradation of nylon PA 66 that involves multiple mechanisms (i.e. plasticization, hydrolysis and swelling) [20,21]. In the presence of moisture, large spaces (as depicted as the large porous areas in Fig. 4.1 a) lead to smooth and easy diffusion for small moisture molecules and eventually plasticization. Plasticization refers to the interruption of van der Waals bonds between polymer chains by the moisture [22]. As a result, the spaces between polymer molecules are further enlarged to accommodate additional water absorption, thereby reducing the interfacial strength of the polymer chains and providing more free movement of the polymer molecules [23].

Hydrolysis is the corresponding chemical reaction which describes the binding of the water molecules to the polymer chains [24-27]. Hydrolysis (Eq.1) causes degradation of the molecular structure by lessening the cohesive mechanics of the molecular network and providing enhanced molecular mobility. Also, the interaction of polar water molecules with the polymer network results in hydrogen bonds with hydroxyl groups in the polymer chain. This bond formation takes place at the cost of varying the inter-chain hydrogen bonding thereby interrupting the polymer chains making nylon brittle.

$$\text{n [-CO-(CH}_2\text{)}_4\text{-CO-NH-(CH}_2\text{)}_6\text{-NH-]} + 2n\ H_2O \rightarrow n\ HO\text{-CO-(CH}_2\text{)}_4\text{-CO-OH} + n\ H_2N\text{-(CH}_2\text{)}_6\text{-NH} \quad (1)\ [28]$$

Further moisture absorption results in swelling of nylon. The swelling stresses act on the vicinity areas leading to micro-cracks development in nylon. These entire phenomena (micro-cracks and nylon embrittlement) weaken the nylon (matrix) causing it separated from the fibers which initiates debonding, as seen in Fig. 4.3 (a).

EDS analysis, presented in Table 3.1, confirms the presence of impurities like Na, Fe, O, Mg and Cl (minerals present in sea water) on the fractured surface. These corrosion products highlight the existence of NaCl and oxides on the fractured surface. However, these products were not absorbed into the resin rather than interacting with its polymer chain, and thus accelerated its deterioration. For instance, NaCl found in this case interacts with the carbonyl

making it more electron withdrawing; and thus, causes the carbon more prone to be attacked by the water, which results in accelerating the entire process. This process is described in Eq. 2 [29].

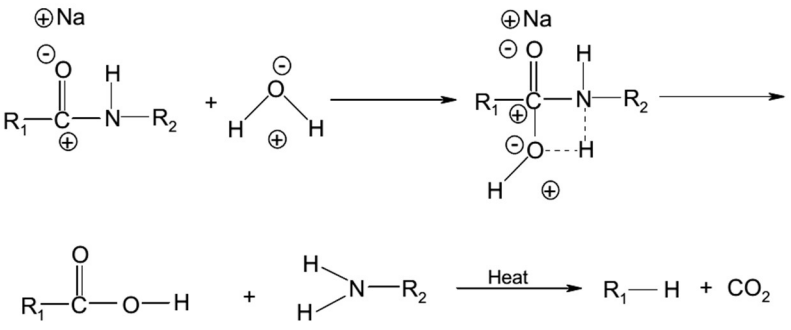

(2) [29]

Table 4.1 Elemental compositions (at. %) in CFRP/Al exposed joints

Na	Fe	O	Mg	Al	Cl	S	C
1.42	2.65	45.21	10.68	5.98	4.81	0.54	28.72
1.19	-	35.62	5.95	3.66	1.79	0.28	51.51
2.47	-	44.74	8.15	5.04	2	-	37.60

To summarize, it is found that CFRP sheet in the exposed CFRP/Al joints fractured due to the mechanical degradation of PA 66 in consequence of the combination of various mechanisms. These mechanisms change the failure mode from fiber pullout and fracture to debonding. The impurities present in the moisture (salts and chlorides) do not react itself with the PA 66 rather serve as catalyst in accelerating the deterioration mechanism.

4.3.2 Exposed FSBR Mg/CFRP joints

4.3.2.1 Mechanical characterization

The exposed Mg/CFRP joints exhibit only tension failure mode (Fig. 4.4 a) in comparison with three failure modes (i.e. tension failure, rivet pull out, and mixed failure) depicted by as-fabricated Mg/CFRP joints [9]. The rusty surface of rivet prevents rivet body to be pulled out during tensile test, which causes the tension failure more easily to happen. Figure 4.4 (b) gives the schematic illustration of this fact, and the fracture took place in CFRP sheet. Mg/CFRP exposed joints have the similar maximum tensile load as the as-fabricated ones but less stiffness.

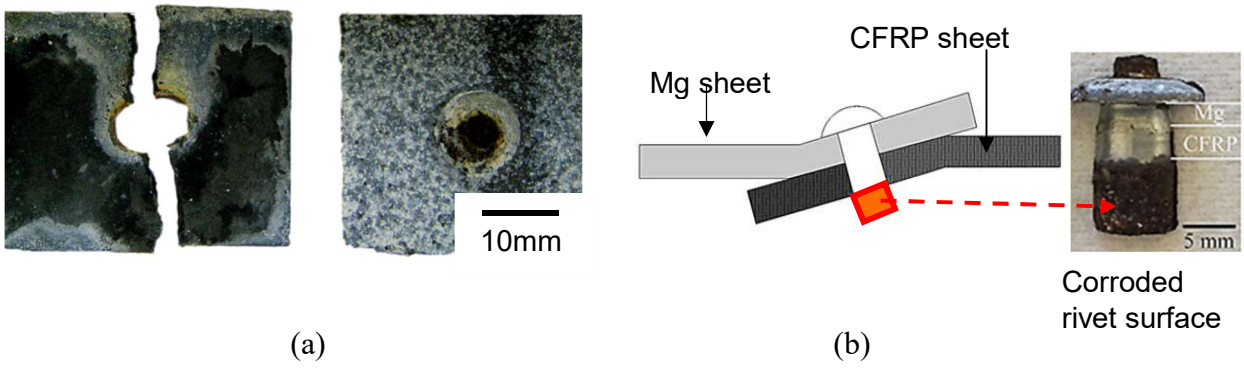

(a) (b)

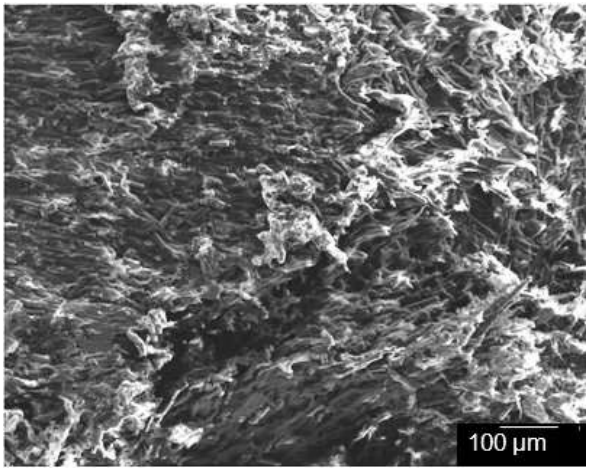

(c)

Figure 4.4 (a) Image of a fractured Mg/CFRP joint in tension failure mode (CFRP fractured), where the white particles are the corrosion products from Mg, (b) rusty surface (highlighted by orange box) that prevents rivet pull out failure, and (c) fractured surface of exposed CFRP sheet where fractured fiber and fiber free of nylon (debonding) is visible

Figure 4.5 (a) shows typical load-displacement curves. It is noted that although the maximum load depicted by the exposed load curve remains almost the same for all exposed joints; however, the elongation has a larger variation from sample to sample which was also seen for the as-fabricated joints. Figure 4.5 (b) compares AE hits between the exposed and as-fabricated Mg/CFRP joints. In the case of Mg/CFRP joints, the sensor was placed on CFRP sheet. As a result, fewer signals were obtained for Mg/CFRP joints than CFRP/Al joints where sensor was placed on Al. The increase in AE hits for exposed joints represents a stepped pattern. Exposed joints generate more hits than as-fabricated joints. The middle portion of the hits curve of the exposed joints raises earlier and much more than as-fabricated joints, indicating more defects and degradation in the exposed joints.

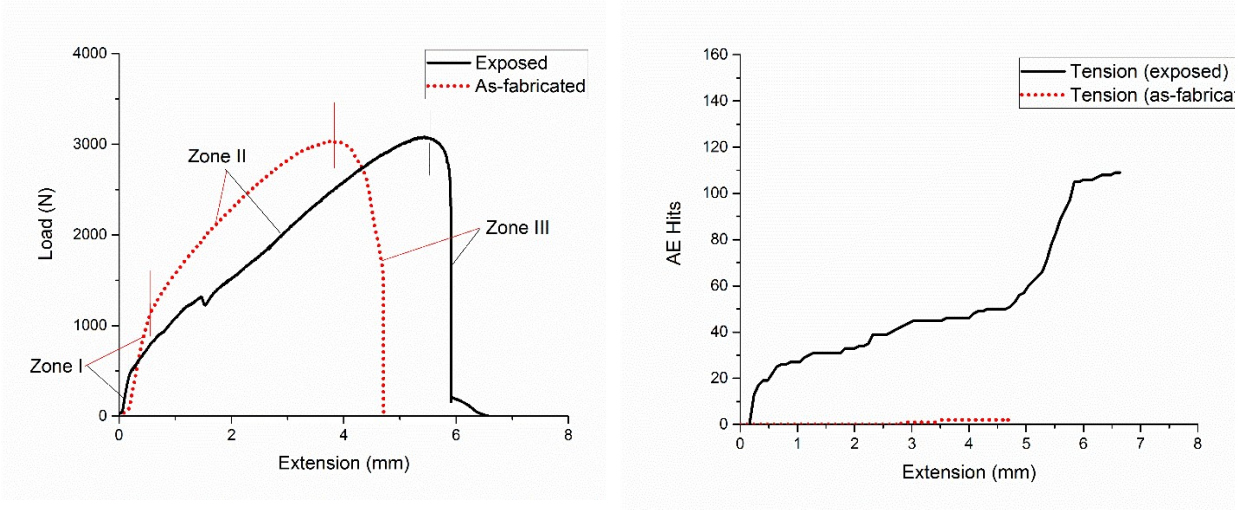

(a) (b)

Figure 4.5 Load-extension and AE accumulative hit curves of the FSBR Mg/CFRP joints: (a) tension failure for exposed and as-fabricated joints, with different zones demarcated by vertical lines, and (b) AE accumulative hits vs extension of as-fabricated and exposed FSBR Mg/CFRP joints showing stepped feature

4.3.2.2 Microstructure

Microstructural analysis of fractured surface reveals debonding and fiber fracture (Fig. 4.4 c). This phenomenon is similar to the microstructural analysis of CFRP sheet in exposed CFRP/Al joint. EDS analysis shown in Table 4.2 revealed Na, Cl, Fe, O along with Ca and Si. Elements like Ca came from sea salt as they are its major constituents. To summarize, fractured CFRP sheet in Mg/CFRP exposed joints also exhibit resin dominant failure mode (debonding) as a result of degradation of nylon's properties which were discussed in detail in section 4.1.1.

Table 4.2 Elemental compositions (at. %) in Mg/CFRP exposed joints

Na	Fe	O	Mg	Al/Ca	Cl	Si	C
8.67	-	8.86	1.8	-/-	6.53	-	74.14
4.85	1.59	53.92	15.47	0.55/-	3.25	-	20.37
18.55	-	39.18	3.8	0.92/10.87	8.79	1.76	16.13

4.3.3 Exposed FSBR Mg/Al joints

4.3.3.1 Mechanical characterization

Two types of failure modes are observed in exposed Mg/Al joints. Figures 4.6 (a) and (b) present bearing followed by rivet pullout and tension, respectively. The direction of the crack (location "A" in Fig. 4.6 b) varies in different samples which is not observed in as-fabricated joints. This is due to the formation of non-uniform corrosion products throughout the surface. Bearing failure occurred for both exposed and as-fabricated joints. However, more materials are removed near the rivet area due to bearing force in exposed joints than the one observed for as-fabricated joints (Fig. 4.6 c). For exposed Mg/Al joints, the bearing stress between rivet body and Mg results in more peeled-off materials (debris) in the vicinity of rivet hole's area than as-fabricated joints because of the brittle nature of the exposed Mg sheet. For as-fabricated joints,

the bearing stress causes plastic deformation in Mg (since it is more ductile, as shown in Fig. 4.6 c) instead of peeling off material and consequently a less hole extension.

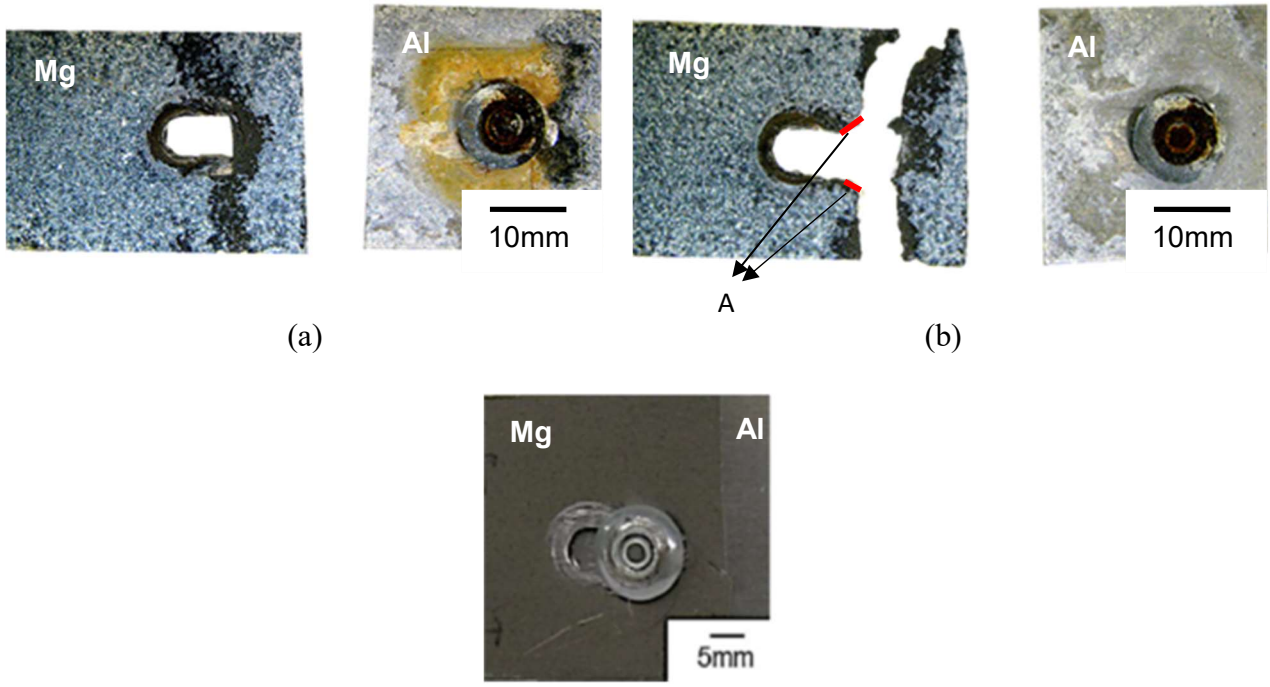

Figure 4.6 (a) Image of an exposed Mg/Al joint in bearing followed by rivet pullout; (b) image of an exposed Mg/Al joints in bearing followed by tension failure mode; and (c) image of as-fabricated FSBR Mg/Al joints in bearing by cleavage failure

The out-of-plane shearing failure area (area "A" in Fig. 4.6 b) is found in both failure modes of exposed Mg/Al samples. The out-of-plane shearing failure area is next to the rivet body. The out-of-plane shear failure is because of the secondary bending, which is caused by an eccentricity of an applied load relative to the neutral axis of a structural component and results in the bending stresses [30]. In exposed Mg/Al FSBR joint, the bending moments on Al and Mg are the same. However, Al (3.6mm thickness) undergoes much smaller bending deformation (amount of bending throughout the sheet) than Mg sheet having 1.7 mm thickness due to lower bending stress caused by different geometries and young's modulus. As a result, Al sheet has

less bending deformation than Mg sheet and the rivet remains perfectly fastened in Al sheet. In current scenario, the bending moment pulled Mg sheet up, as the bending results in a force in an out-of-plane direction, whereas, the rivet head applied a shearing force on the area near the edge of rivet head. Due to brittleness of exposed Mg, the material fractured in the rivet head's edge vicinity resulting in an out-of-plane shear failure. In as-fabricated samples, the Mg sheet near rivet head's edge undergoes plastic deformation instead of fracture (due to ductile nature of Mg) under out-of-plane shear force.

The failure modes can be classified in two types depending on the size of out-of-plane shearing failure area. When the size of the crack is larger than rivet head, the rivet head can be pulled out from Mg sheet (pullout failure). On the other hand, a smaller crack size yields tension failure with a non-flat surface. The mechanical behavior of FSBR Mg/Al joints in the form of load-extension and AE accumulative hit curves are summarized in Fig. 4.7. Four deformation zones are identified for this material combination (Fig. 4.7 a), which are categorized as Zone I, Zone II, Zone III, and Zone IV [9], presenting linear elastic deformation, first non-linear plastic deformation region till the maximum tensile load peak, the second plastic deformation region till the second maximum tensile load peak, and the unstable deformation till final facture, respectively. The maximum load for the exposed joints appears at the first peak in Zone II. This is different from as-fabricated joints, where the maximum load occurred at the second peak. In exposed Mg/Al joints, the first peak has the maximum load. This is because the exposed Mg is brittle, the material in bearing area was crushed into debris; whereas for the as-fabricated samples, the first peak highlights the initiation of crack after which there is a load drop and the maximum load appears at second peak when the fracture happened. The maximum load for the exposed joints (failed in tension mode) is 5331 N. This implies in a decreased strength of exposed joints compared to as-fabricated ones where the maximum load is 6139N. The exposed joints, however, have larger extensions primarily because of the extended hole generated by the combination of bearing and bending stress. It was found that the exposed joints have a smaller threshold elastic region (Zone I) than as-fabricated joints. For the exposed joints, during the bearing process (Zone II), Mg debris peeled off by rivet body from bearing area are brittle and small, and can come out from bearing area easily. Therefore, the load curve depicts a linear behavior. For Zone III, the load extension curve of the exposed samples exhibits three small peaks. This can be correlated with the stepped fracture surface discussed earlier (section 4.1.3).

The three peaks indicate that the tension test was not abrupt and there was shifting of load due to different contact regions between differently stressed areas. Finally, the end of Zone IV marks the fracture of Mg sheet. The load curve shows a relatively smoother load drop than as-fabricated joints before dropping to zero. This load drop is caused by the continuous frictional contact between the Al and rough corroded Mg surfaces. This feature is not visible in as-fabricated joints load curves, where both Al and Mg have smooth surfaces. Figure 4.7 (b) compares the AE accumulative hit evolutions for both as-fabricated and exposed joints. The elongation (i.e. deformation time at a fixed loading speed) for the exposed joints is more than as-fabricated joints. This is because the exposed joints always have bearing before other failures occurred. A larger number of hits are observed for exposed joints than the as-fabricated joints confirming the presence of various failure mechanisms like peeling of more material due to a large bearing distance and shifting of load as a result of non-uniform corrosion products. Besides, the hit curves of the exposed joints start to rise earlier than as-fabricated joints as Mg fragments peeled off during bearing in the exposed joints.

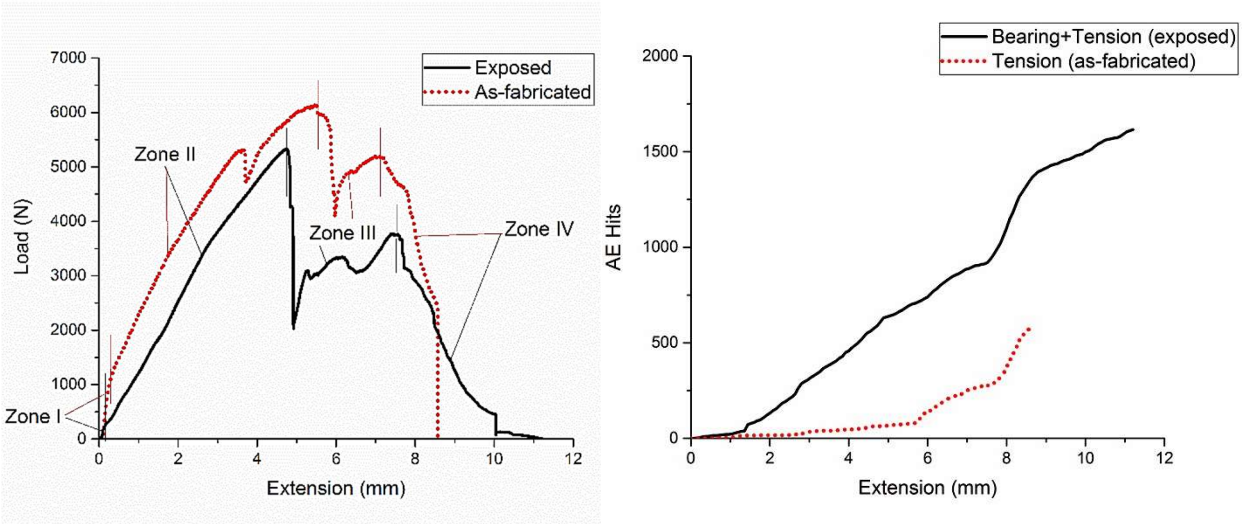

(a) (b)

Figure 4.7 Load-extension and AE accumulative hit curves of the FSBR Mg/Al joints: (a) load curves showing different zones for corroded and as-fabricated joints where vertical lines, and (b) AE accumulative hits vs extension curve showing more signals for corroded joints

4.3.3.2 Microstructure

Figure 4.8 (a) (cross section from location "A" in Fig 4.6 b) highlights the fracture surface of Mg sheet with the shearing failure. The stepped surface is caused by the continuous change of loading which varies the crack direction and subsequently the stressed area. SEM analysis shows brittle corrosion products on fractured Mg surface. Numerous acicular clusters were found on the surface (Fig. 4.8 b). The presence of acicular structures throughout the fractured surface points that their presence is not because of sample preparation for SEM analysis. Acicular clusters were also found by Cui et al. [31] and Lindstrom et al. [32] in the studies on magnesium alloys in the laboratory atmospheric exposure and immersion tests.

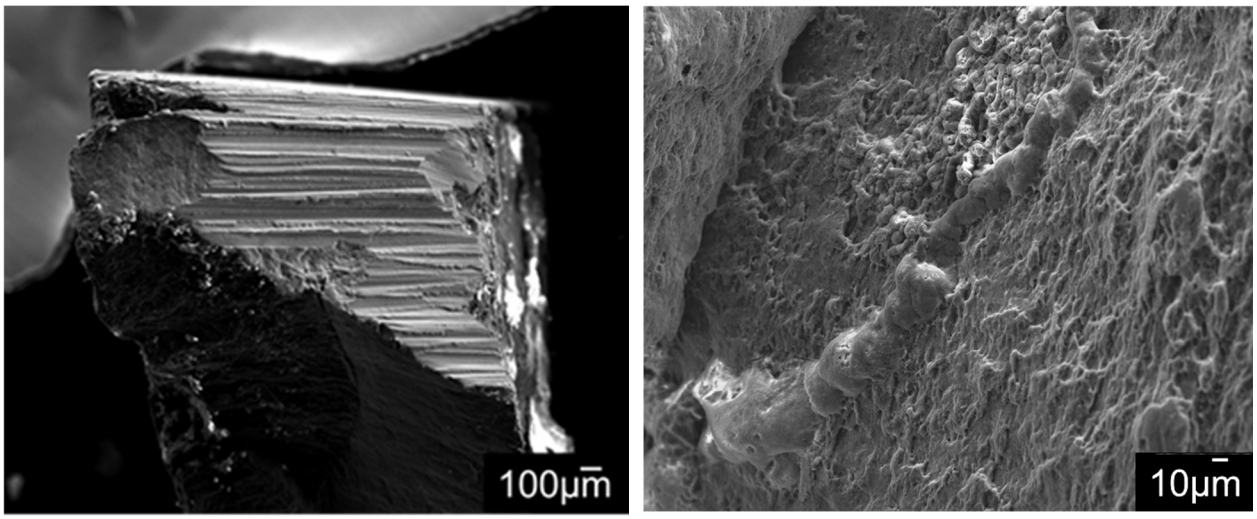

(a) (b)

Figure 4.8 Microstructural analysis of exposed Mg/Al joint: (a) fractured surface of magnesium sheet, and (b) acicular products results due to formation of chloride ions

From the EDS analysis, corrosion products include Cl, O, Na, Al, Si and C. The acicular products found to be composed of Cl and O. The presence of Cl containing particles highlights the formation of thin adsorbed electrolyte layer consisting of chloride ions.

Table 4.3 Elemental compositions (at. %) in Mg/Al exposed joints

C	O	Na	Mg	Al	Cl	Si
22.78	13.29	0.47	61.4	1.64	-	22.78
15.28	32.77	-	35.22	-	16.73	-
-	56.26	-	33.54	-	10.2	-

4.4 Discussion on the degradation of mechanical properties

From the previous discussion, it is observed that the maximum tensile load of the Mg/CFRP and CFRP/Al FSBR joints does not change after exposure to marine environment. However, there is a 15.1 % loss in maximum tensile load in Mg/Al joints after exposure to marine environment. On the other hand, there is a significant loss in nominal stiffness observed in all the three configurations upon exposure. Figure 4.9 gives the comparison of mean nominal stiffness of three configurations whereas the % loss in nominal stiffness for the three configurations is calculated by Eq. 3.

$$\%\ Loss\ of\ nominal\ stiffness = \frac{Nominal\ stiffness\ of\ as-fabricated\ joint - Nominal\ stiffness\ of\ exposed\ joint}{Nominal\ stiffness\ of\ as-fabricated\ joint} \quad (3)$$

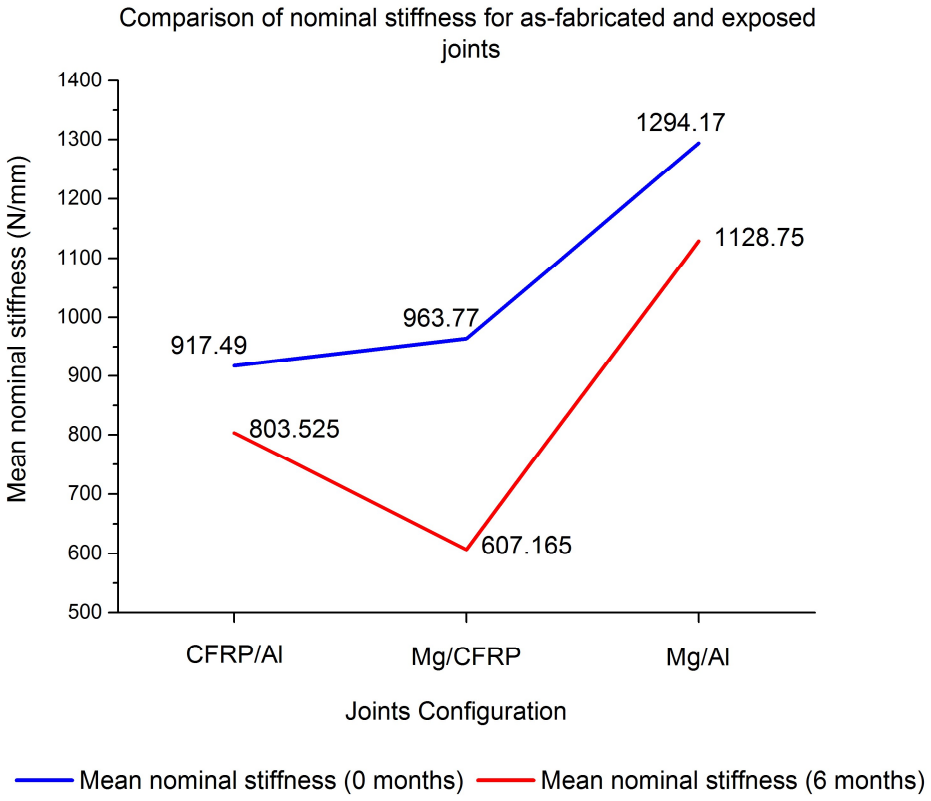

Figure 4.9 Comparison of mean nominal stiffness for the three configurations (considering as-fabricated and 6 months exposed samples)

Two main observations are drawn from the analysis. Firstly, it can be inferred that CFRP/Al and Mg/Al exposed joints have similar % loss in nominal stiffness. As Al is the common material in both the configurations and failure in CFRP/Al and Mg/Al occurred in CFRP and Mg, respectively (Al sheet does not fail in both the cases). To identify the mechanical property changes in exposed CFRP, Mg and Al, a series of tensile tests were conducted. Firstly, tensile tests on as-received and exposed Al sheets were performed to examine the % loss in nominal stiffness. Secondly, tensile tests on exposed Mg and CFRP sheets, taken from Mg/Al and CFRP/Al exposed joints, were conducted to see if they exhibit the similar nominal stiffness. Results of both tests are presented in Fig. 4.10. Figure 4.10 (a) displays the tensile test results of exposed and as-received Al sheets, where the load-extension curves of as-received Al sheets are presented in terms of mean and standard deviation. It can be seen that load-extension curves for

both the exposed Al sheets, joined with CFRP and Mg, lie within the range of as-fabricated Al sheets confirming that there is negligible loss in nominal stiffness of Al in the current corrosion environment. Figure 4.10 (b) compares the load-extension curves for exposed CFRP and Mg, taken from exposed CFRP/Al and Mg/Al joints. It is evident that these two materials have the similar nominal stiffness.

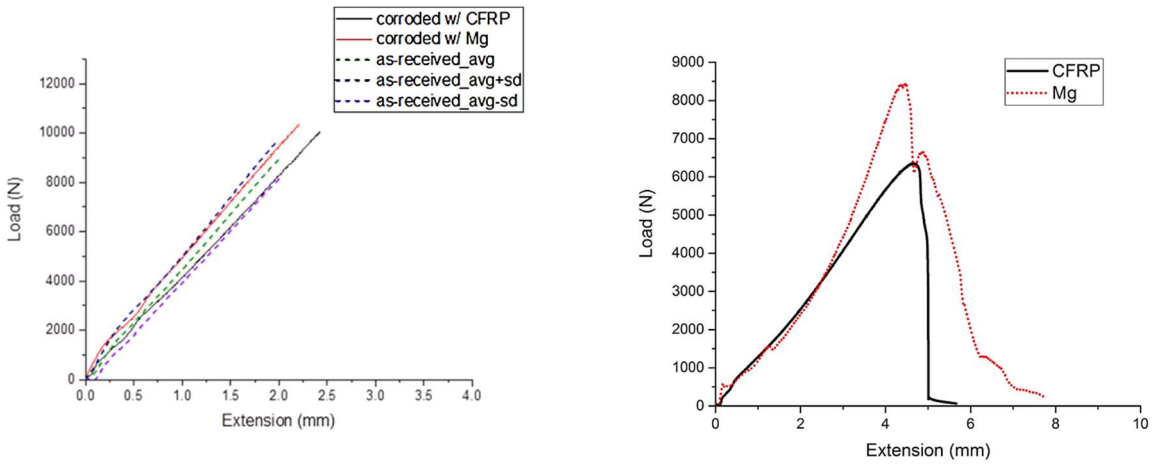

(a) (b)

Figure 4.10 Load-extension curves to examine nominal stiffness in Al, CFRP and Mg after exposure: (a) load-extension curves of corroded and as-received Al showing the nominal stiffness of corroded Al sheets falls within one standard deviation of as-received Al value; and (b) load-extension curves of corroded CFRP and Mg sheets showing similar nominal stiffness

Secondly, %loss in nominal stiffness is approximately three times for exposed Mg/CFRP joints as the other two exposed joints configurations (i.e., % stiffness loss in Mg/CFRP exposed joints is 37 % in comparison to 12.42% and 12.78% for CFRP/Al and Mg/CFRP exposed joints respectively). The possible reason for this behavior is the electrode potential difference between Mg-CFRP is higher than the values in CFRP-Al and Mg-Al. Moreover, absorbed energy for all these three joint configurations during tensile test till fracture is calculated. Energy calculations reveal that the absorbed energy increases for the joints when exposed to marine environment. All the three joint configurations present the same trend. The average energy absorbed for CFRP/ Al exposed joints is 57.47 J compared to 28.96 J of as-fabricated ones, whereas for exposed

Mg/CFRP it is 23.87 J compared to 18.22 J in as-fabricated samples. For Mg/Al configuration, the average absorbed energy is 59.69 J and 51.48 J for exposed and as-fabricated joints, respectively. It is pertinent to mention that for the exposed joints having a CFRP sheet, the maximum displacement values are higher than as-fabricated ones (Figs. 4.2 a and 4.5 a) because of plasticization which resulted in more elongations at break and higher toughness [33]. This phenomenon resulted in high absorbed energy values. For Mg/Al exposed joints larger extensions are primarily because of the extended hole generated by the combination of bearing and bending stress which resulted in an increase in absorbed energy.

4.5 Conclusions

The current paper has evaluated the mechanical behavior (i.e. maximum tensile load, maximum elongation to break, energy dissipated, and nominal stiffness) and failure modes of FSBR dissimilar materials joints under uniaxial tensile tests to assess the changes in mechanical properties introduced by corrosive marine environment.

For joints containing CFRP material, CFRP sheet undergone fracture. Load curves of both CFRP/Al and Mg/CFRP exposed joints display similar strength but less stiffness when compared with their as-fabricated counter parts. Visual observations revealed that the steel rivet area interacting with the interface of the two member sheets did not undergo corrosion thus serving as key contributing factor for the similar strengths. However, less stiffness is attributed to polymer chain interaction with moisture, corrosion products and growth of micro cracks which ultimately leads to debonding. Microstructure analysis revealed debonding as the main failure mode of CFRP sheets as a consequence of nylon weakening because of plasticization, hydrolysis and swelling phenomena. Corrosion products like NaCl found on the fracture surface did not react with the nylon but accelerated the process of polymer degradation.

Failure modes observed in exposed Mg/Al joints are bearing followed by tension and rivet pullout. An out-of-plane shearing failure area, next to the rivet body, was found in both failure modes of exposed Mg/Al joints. Stepped pattern for the fractured Mg surface, observed in microstructural analysis, was caused by the continuous change of loading conditions and subsequently the stressed area. Load curve for the exposed Mg/Al joint exhibit different peak

load locations and load drop patterns than as-fabricated Mg/Al joints because of the load shift and brittle nature of Mg.

By evaluating the nominal stiffness, it was found that CFRP/Al and Mg/Al exhibits similar loss of nominal stiffness. Since, Al is the common material in both the cases, with negligible stiffness loss, it is concluded through experiments that the CFRP and Mg have similar % loss of nominal stiffness. This was also confirmed from the tensile tests of exposed Mg and CFRP sheets. The % loss of nominal stiffness in exposed Mg/CFRP was found almost twice than the other two joint configurations. The absorbed energy values in all the exposed configurations are higher than their as-fabricated counterparts. The prime reasons for this factor are plasticization in CFRP sheet and a large hole extension in Mg (in case of Mg/Al exposed joints) due to brittleness of Mg.

REFERENCES

[1] Shahri, M.M., Sandström, R., 2012. Influence of fabrication stresses on fatigue life of friction stir welded aluminum profiles. Journal of Materials Processing Technology. 212, 1488-1494.

[2] Min, J., Li, Y., Li, J., Carlson, B. E., Lin, J., 2015.Mechanics in frictional penetration with a blind rivet. Journal of Materials Processing Technology. 222, 268-279.

[3] Gao, D., Ersoy, U., Stevenson, R., Wang, P.C., 2009. A New One-Sided Joining Process for Aluminum Alloys: Friction Stir Blind Riveting. Journal of Manufacturing Science and Engineering, 131, 061002–61011.

[4] Min, J., Li, J., Li, Y., Carlson, B. E., Lin, J., Wang, W. M., 2015. Friction stir blind riveting for aluminum alloy sheets. Journal of Materials Processing Technology. 215, 20-29.

[5] Min, J., Li, Y., Li, J., Carlson, B. E., Lin, J., 2015. Friction stir blind riveting of carbon fiber reinforced polymer composite and aluminum alloy sheets. The International Journal of Advanced Manufacturing Technology. 76. 1403-1410.

[6] Min, J., Li, J., Carlson, B. E., Li, Y., Quinn, J. F. , Lin, J., Wang ,W.M.,2015. Friction Stir Blind Riveting for Dissimilar Cast Mg AM60 and Al alloy Sheets. ASME Journal of Manufacturing Science and Engineering.137, 1022-1029.

[7] Min, J., Li, J., Li, Y., Carlson, B. E., Lin, J., 2014. Mechanical property of Al alloy joints by friction stir blind riveting. Procedia Engineering. 81. 2036-2041.

[8] Lathabai, S., Tyagi, V., Ritchie, D., Kearney, T., Finnin, B., 2011. Friction Stir Blind

Riveting: A Novel Joining Process for Automotive Light Alloys. SAE2011-01-0477.

[9] Wang, W.M., Khan, H.A., Li, J.J., Miller, S.F., Zachary, T. A., 2017. Classification of Failure Modes in Friction Stir Blind Riveted Lap-Shear Joints with Dissimilar Materials. Journal of Manufacturing Science and Engineering. 139. 021005-1.

[10] Li, S., Khan, H., Hiharaa, L.H., Li, J.J., 2016. Marine Atmospheric Corrosion of Al-Mg Joints by Friction Stir Blind Riveting. Corrosion Science. 111. 793-801.

[11] Srinivasan, R., Hihara, L., 2015. Development of Guidelines to Attenuate Galvanic Corrosion between Mechanically-Coupled Aluminum and Carbon-Fiber Reinforced Epoxy Composites Using Insulation Layers. Journal of the Electrochemical Society. 162. 545-554.

[12] Gebhard, A., Bayerl, T., Schlarb, A. K., Friedrich, K., 2009. Galvanic corrosion of polyacrylnitrile (PAN) and pitch-based short carbon fibers in polyetheretherketone (PEEK) composites. Corrosion Science. 51. 2524-2528.

[13] Mandel, M., Krüger, L., 2013. Determination of pitting sensitivity of the aluminum alloy EN AW-6060-T6 in a carbon-fiber reinforced plastic/aluminum rivet joint by finite element simulation of the galvanic corrosion process. Corrosion Science. 73. 172-180.

[14] Bardal, E., 2004. Corrosion and protection, Spriger Verlab, Berlin.

[15] Calabrese, L., Proverbio, E., Pollicino, E., Galtieri, G., Borsellino, C., 2015. Effect of galvanic corrosion on durability of aluminum / steel self-piercing rivet joints. Corrosion Engineering Science and Technology. 50. 10-17.

[16] Min, J., Li, J., Carlson, B.E., Li, Y., Lin, J., 2014. Mechanical property of Al alloy joints by friction stir blind riveting. Procedia Engineering. 2036-2041.

[17] Abedrabbo, N., Pourboghrat, F., Carsley, J., 2007.Forming of AA5182-O and AA5754-O at elevated temperatures using coupled thermo-mechanical finite element models. International Journal of Plasticity. 23. 841–875.

[18] Accessed at: http://www.matweb.com/search/DataSheet.aspx

[19] Product development report of NN-40CF/000 BLACK (provided by PolyOne™).

[20] George, S.C, Thomas, S., 2001. Transport phenomena through polymeric systems. Progress in Polymer Science. 26. 985-1017.

[21] Wong, K.J., 2013. Moisture absorption characteristics and effects on mechanical behavior of carbon/epoxy composite: application to bonded patch repairs of composite structures. Universit´e de Bourgogne.

[22] Wolff, E.G., 1993.Moisture effects on polymer matrix composites. SAMPE Journal. 29(3).11-19.

[23] Lv, X.J., Zhang, Q., Li, X.F., Xie, G.J., 2008. Study of the influence of immersion on the carbon fiber/epoxy composites. Journal of Reinforced Plastics and Composites. 27(6). 659-666.

[24] Anda, A., R., 2012. Influence of the solvent sorption, additivation, and chemical modification on the molecular mobility dynamics of Polyamide 6, 6 amorphous phase and its consequences on the tensile and impact strength properties of this polymer. Universit´e Claude Bernard- Lyon I.

[25] Murthy, N., S., 2006. Hydrogen Bonding, Mobility, and Structural Transitions in Aliphatic Polyamides, J. Polym. Sci. Part B: Polym. Phys. 44. 1763.

[26] Iwamoto, R., Murase, H., 2003.Infrared Spectroscopic Study of the Interactions of Nylon-6 with Water, J. Polym. Sci. Part B: Polym. Phys. 41. 1722.

[27] Rastogi, S., Terry, A., E., Vinken, E., 2004.Dissolution of Hydrogen-Bonded Polymers in Water: A Study of Nylon-4, 6, Macromolecules. 37. 8825.

[28] Papanicolaou,G.C.,Kosmidou,T.V.,Vatalis,A.,S.,Delides,C.,G.,2006.Water absorption mechanism and some anomalous effects on the mechanical and viscoelastic behavior of an epoxy system. Journal of Applied Polymer Science. 99. 1328-1339.

[29] Steward, S., 1999.The Effect of Salt Splash on Nylon 6, 6. Virginia Polytechnic Institute and State University Blacksburg, Virginia, USA.

[30] Skorupa, M., Korbel, A., 2008.Modelling the secondary bending in riveted joints with eccentricities. The archive of mechanical engineering.4.369-387.

[31] Cui, Z., Li, X., Xiao, K., Dong, C., 2013.Atmospheric corrosion of field-exposed AZ31 magnesium in a tropical marine environment. Corrosion Science.76.243-256.

[32] Lindström, R., Johansson, L. G., Svensson, J. E., 2003. The influence of NaCl and CO_2 on the atmospheric corrosion of magnesium alloy AZ91.Materials and Corrosion.54.587-594.

[33] Immergut, E.H., Mark, H., 1965.Principles of plasticization. Polytechnic institute of Brooklyn, Brooklyn, N. Y., USA.

CHAPTER 5

CONCLUSIONS AND FUTURE WORK

5.1 Conclusions

This dissertation investigated the FSBR process through SPH-FEM simulation and the mechanical behavior of three different FSBR lap joints (before and after marine atmospheric corrosion) by experimental analysis. A numerical model developed with mesh-free elements was created to study material flow and working temperature of Mg/Al FSBR joint. This partial 3-D model was less computationally expensive compared to a complete 3D model. The predicted results have good agreements with the experiment according to thrust forces and formation of interlock. Six different failure modes were identified for these three FSBR joints subjected to tensile loading. AE accumulative hit history curve was found to be an efficient method to discriminate the deformation characteristics and forecast the final failure. To understand degradation in mechanical behavior, FSBR joints were also exposed in marine atmospheric corrosive environments for six months. Both SEM analysis and tensile tests along with AE sensing were conducted to characterize corrosion products and mechanical properties.

5.1.1 Numerical analysis for FSBR process

The partial 3-D model is proved to be the most economic method to simulate the FSBR process that evolves large deformations and complex thermomechanical phenomena. In addition, two different materials were being penetrated by a complex-shape rivet, which further raised the simulation challenge. The mesh-free SPH elements can address these difficulties and predict the histories of material flow, internal temperature, stress and pressure along with the process. All these parameters could not be quantified through experiment. The formation of interlock was also predicted with a good agreement with microstructure.

5.1.2 Mechanical behavior of dissimilar FSBR joints

The failure modes of dissimilar as-fabricated FSBR joints (Mg/Al, Mg/CFRP, and CFRP/Al) were identified. The load-extension and accumulative hit curve charts effectively presented the deformation characteristics, such as deformation zone and failure mode. Different dominate failure zones for each type of joints can be predicted through AE signals. It was found that the failure modes of dissimilar FSBR joints were related to the interlock at interface (material flow) which was generated during FSBR process. It was found tension and cleavage failures occurred in the CFRP workpiece for as-fabricated CFRP/Al FSBR joints; tension, shearing, and bearing followed by cleavage failure modes in Mg/Al joints; and tension failure on CFRP, mixed failure of tension and shearing on Mg, or rivet pullout happened in CFRP/Mg joints.

5.1.3 Mechanical characteristics of FSBR joints exposed to marine environment

The effects of marine environment on mechanical properties and failure modes of FSBR dissimilar materials joints were investigated, where the three material combinations included Mg/Al, Mg/CFRP, and CFRP/Al. For CFRP constituent exposed joints, the dominated failure mode was tension failure and showed no loss in strength under current corrosion condition. Exposed Mg/Al joints depicted a complex failure mode caused by secondary bending and bearing force, and degradation in strength was observed. In addition, through the analysis of nominal stiffness, it was found that CFRP and Mg sheets underwent a similar loss of nominal stiffness whereas there is no significant stiffness loss in individual aluminum sheets.

5.1.4 Contributions

The major contributions of this dissertation can be summarized as the following:

- The partial model is a suitable approach to reduce the computational time of the FSBR SPH-FEM model. Besides, this study presents how to develop an effective numerical model for friction stir process when the tool geometry is complex.

- Material flow and temperature profile of workpieces in FSBR process are identified through the numerical model, which cannot be observed from experiment directly and thus can help the researchers to understand the process physics more deeply.
- The failure mechanisms of dissimilar FSBR joints can be valuable for a better joint design.
- AE hit is found to be a convenient tool to detect and predict the failure mode of FSBR joints.
- Effects of corrosion on mechanical properties and failure modes of FSBR dissimilar joints are identified. After corrosion, the different failure modes should be considered in the future design.
- After 6-month exposure, the strength of CFRP/Al or Mg/CFRP FSBR lap joints is maintained since the interface between rivet and workpieces remains uncorded. This indicates that FSBR joints have better mechanical properties than conventional blind rivet joints in corrosive environment.

5.2 Future work

1. To broaden the application of FSBR for various industries, mechanical behavior of FSBR joints under different loading conditions should be investigated, such as dynamic loading. The deformation and failure modes of FSBR joints under different loading conditions should be different with traditional blind riveting joints because of the mechanical locking and bonding between rivet and work materials generated by friction stir process.
2. Three-layer FSBR joint (double-lap joint) needs to be studied. Double-lap joints can prevent the secondary bending of lap joints; and thus could have a wide application. The stack-up sequence of three layers in FSBR process should be the focus in the study.
3. Designing a new blind rivet could improve the performance of the FSBR process. The new rivet design could decrease the spindle speed and stimulate feed rate, and thus to reduce the consumed energy and accelerate the whole process. The new design is not only on tool geometry but also coating to further reduce the corrosion between dissimilar materials.

4. Numerical model for CFRP/Al FSBR process needs to be created. In this dissertation, the mechanical interlocking in CFRP/Al joints is large and acts as an important role on joint strength. The main challenge for this work is that Johnson-Cook model is not a proper model for CFRP.